

1 Internal Tides–Cyclonic Eddy Interaction and Intermodal 2 Energy Pathways: Evidence from 3-km NEMO-AMAZON36 3 Simulations

4 Fabius Kouogang^{1,2}, Ariane Koch-Larrouy¹, Xavier Carton³, Fernand Assene⁴, Guillaume
5 Morvan⁵, Moacyr Araujo²

6 ¹CECI, Université de Toulouse, CERFACS/CNRS/IRD, Toulouse, France

7 ²Departamento de Oceanografia, Universidade Federal de Pernambuco, DOCEAN/UFPE, Recife, Brazil

8 ³Physical and Spatial Oceanography Laboratory, European Institute for Marine Studies, University of Western
9 Brittany, Plouzane, France

10 ⁴Department of Maritime Navigation and Information System, National Advanced School of Maritime and Ocean
11 Science and Technology (NASMOST), University of Ebolowa, Kribi, Cameroon

12 ⁵Université de Toulouse, LEGOS (CNES/CNRS/IRD/UT3), Toulouse, France

13 *Correspondence to:* Fabius Kouogang (fabius.cedric@yahoo.fr)

14 **Abstract.** The interaction between internal tides (ITs) and mesoscale features plays a key role in ocean energy
15 dissipation. Understanding how IT energy is transformed in energetic western boundary regions remains a central
16 challenge, particularly in regions of vigorous mesoscale activity.

17 To this aim, we apply vertical mode decompositions to the high-resolution (3 km) simulations during September-
18 December 2015. This study shows that the IT vertical mode and the precise point of IT-eddy encounter determine
19 whether the IT energy propagates freely, deviates, or is trapped, and how topography and coherent eddies
20 synergistically scatter energy between baroclinic modes off the Amazon shelf.

21 Three representative interaction cases, each captured in a separated 25 hour snapshot, were examined: undisturbed
22 propagation until crossing the Ceará Rise seamount, interaction with a cyclonic eddy (CE) core, and interaction
23 with a CE eastern edge. The principal findings establish two points.

24 First, an IT response (propagation, deviation or scattering) is dually controlled by its vertical mode, and the
25 mesoscale encounter location along with the associated background conditions (currents and stratification). In the
26 absence of a strong eddy, the Mode-1 IT propagates as a coherent beam with a long propagation range (O (1100
27 km)). In the presence of a strong CE, however, the IT beams are disrupted, preventing sustained long-range
28 transmission. Within the eddy core, the Mode-1 IT is coherently refracted northward ($\sim 35^\circ$ relative to its
29 northeastward incident direction) while maintaining high energy fluxes exceeding 200 W m^{-1} . At the CE edge,
30 Mode-1 is diffracted into two distinct branches, with one propagating northward ($\sim 39^\circ$) and the other eastward
31 ($\sim 35^\circ$). In contrast, the IT higher modes are highly susceptible to blocking and trapping: Mode-2 energy, despite
32 initial amplitudes comparable to Mode-1, is strongly blocked at the CE-seamount interface, while Mode-3 remains
33 weak (below 200 W m^{-1}) and less propagative.

34 Second, intermodal energy transfer is governed by a hierarchical synergy between the seamount and CE's
35 background flow. In the absence of an eddy, the seamount drives a forward energy cascade (O ($10^{-8} \text{ W m kg}^{-1}$))
36 from the Mode-1 IT to higher modes. In contrast, in the presence of a CE, the CE's strong horizontal shear triggers

37 a competing inverse energy cascade ($O(10^{-8} \text{ W m kg}^{-1})$) from the background flow to the IT modes. This
38 interaction is critical for the extreme damping of Mode-2 and explains the observed redistribution of energy fluxes.
39 These results provide mechanistic insight into the fate of IT energy in complex oceanic environments and advance
40 understanding of multi-scale ocean dynamics.

41 **1 Introduction**

42 Internal tides (ITs)—internal waves at tidal frequencies—are generated when barotropic tides interact with
43 topography, forcing vertical displacements of the stratified water column (Garrett and Kunze, 2007; Kelly and
44 Nash, 2010; Buijsman et al., 2012; Zhao, 2014; Chen et al., 2022). They enhance turbulent mixing and influence
45 deep-water circulation (Wunsch and Ferrari, 2004; Kunze, 2017).

46 High-mode ITs, characterized by short wavelengths and large vertical shear, typically dissipate near their
47 generation sites (Vic et al., 2019; Koch-Larrouy et al., 2015; Kouogang et al., 2025). In contrast, low-mode ITs
48 propagate thousands of kilometers, redistributing tidal energy and acting on open-ocean mixing (Zhao, 2017;
49 Alford et al., 2019; Wang et al., 2021; Kouogang et al., 2025). During their propagation, ITs can interfere with
50 other tidal beams (e.g., tidal beams from other sources), interact with oceanic flows (e.g., subtidal currents,
51 mesoscale eddies) and topography (e.g., seamounts, ridges), generating nonlinear internal solitary waves (ISWs)
52 (Pereira et al., 2007; Zhang et al., 2014; Kelly and Lermusiaux, 2016; Wang et al., 2021; Xu et al., 2021; Wang
53 et al., 2024; Li et al., 2024). Low-mode ITs can be scattered into higher modes by bathymetric roughness (Johnston
54 and Merryfield, 2003; Mathur et al., 2014). These multiscale interactions cause IT incoherence and nonstationary,
55 challenging satellite detection (Zaron and Egbert, 2014; Savage et al., 2020).

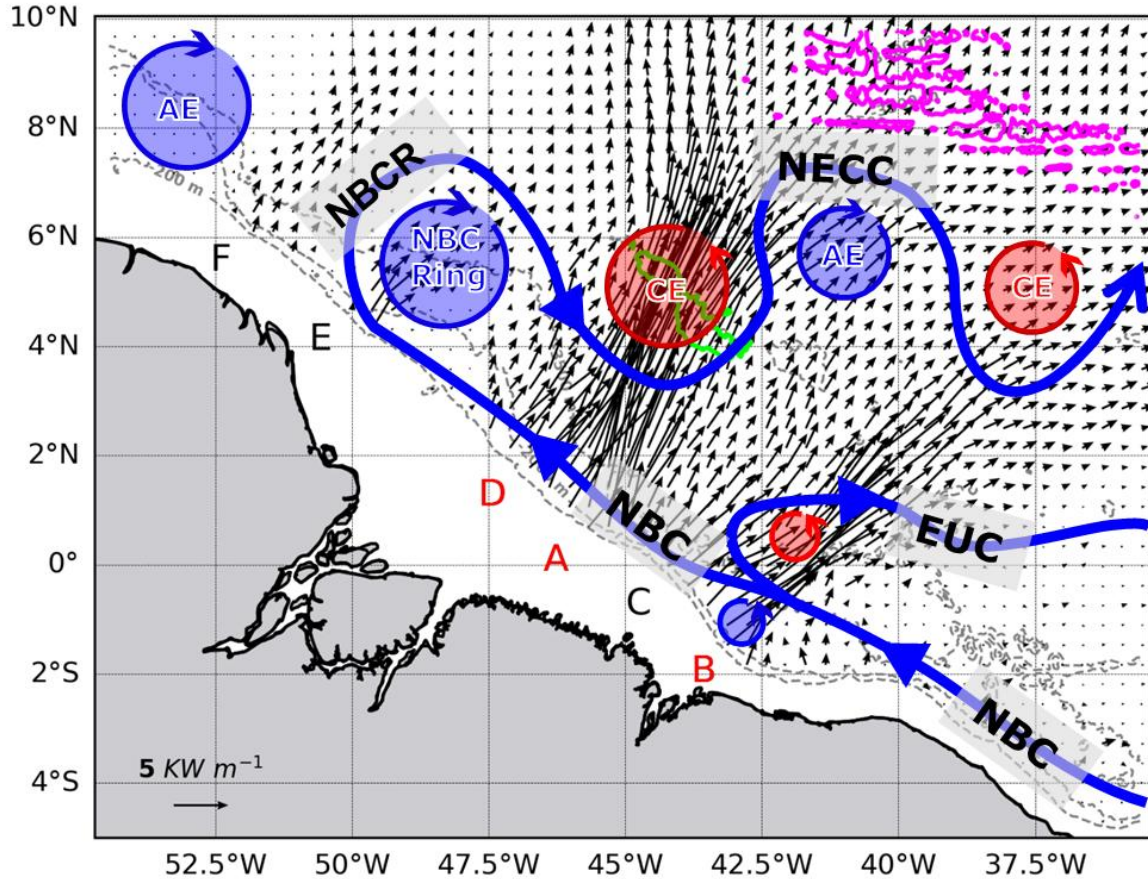
56 Mesoscale eddies (MEs)—comprising both anticyclonic (AEs) and cyclonic (CEs) types—often possess
57 horizontal scales comparable to those of low-mode ITs. This scale similarity allows MEs to alter oceanic
58 stratification and currents, thereby influencing IT generation, propagation, and inter-modal energy redistribution
59 through processes such as scattering, refraction, trapping, and damping (Dunphy and Lamb, 2014; Clément et al.,
60 2016; Dunphy et al., 2017; Guo et al., 2023; Wang and Legg, 2023). MEs can enhance or weaken the topography
61 scattering of ITs, causing spatial divergence (Li et al., 2024). Low-mode ITs can also be refracted or trapped by
62 background currents like the looping and leaping Gulf Stream (Duda et al., 2018; Kelly and Lermusiaux, 2016;
63 Kelly et al., 2016), Kuroshio (Cao et al., 2022; Xu et al., 2021; Chen et al., 2022) and Brazil Current (Pereira et
64 al., 2007), changing their direction of propagation (Huang et al., 2018). Scattering by topography and background
65 circulation to higher modes can redistribute energy toward more dissipative pathways (Lahaye et al., 2020; Fan
66 et al., 2024).

67 Although the IT responses to background circulation (stratification, currents, and eddies) are well-documented on
68 seasonal and interannual timescales (Pereira et al., 2007; Nash et al., 2012; Tchilibou et al., 2020, 2022), their
69 variability at shorter, daily timescales remains less explored. On seasonal timescales, it becomes difficult to
70 distinguish variations in IT responses (e.g., incoherence, trapping, and deviation), particularly those induced by
71 changes in submesoscale and mesoscale activity, and background shear. Analyses at daily timescales could better
72 capture the specific background conditions that most strongly modulate the fate of ITs. Our study addresses this
73 issue by investigating the rapid variability of IT responses to MEs off the Amazon shelf.

74 The region off the Amazon shelf is a dynamic region with a strong western boundary current (North Brazil
75 Current, NBC), receiving large amounts of freshwater from the Amazon and Para Rivers. The area is also marked

76 by high mesoscale activity (MEs), and the presence of seamounts, ITs, and ISWs (Fig. 1). The NBC flows
77 northwestward, exhibiting a seasonal double retroflexion eastward, a first one into the North Equatorial Counter-
78 Current (NECC) at about 5–8° N near 50° W, and a second one into the Equatorial Undercurrent (EUC) in winter–
79 spring (Didden and Schott, 1993). Shear instabilities within these currents and their interaction with the Amazon
80 slope generate the CEs and AEs (NBC rings) in this region (Fratantoni and Glickson, 2002; Barnier et al., 2001;
81 Silva et al., 2009). From August to December (ASOND), mean currents and eddy kinetic energy (EKE) are
82 stronger, and the pycnocline is deeper and weaker than during the March-to-July (MAMJJ) season (Aguedjou et
83 al., 2019; Barbot et al., 2021; Tchilibou et al., 2022). Generated at multiple sites (A to E, Fig. 1) along the Amazon
84 shelf break (Tchilibou et al., 2022; Assene et al., 2024; Magalhaes et al. 2016), ITs from the most energetic sites
85 (A and D, Fig. 1) can either propagate over long distances or interact with other processes to potentially
86 disintegrate into ISWs, which have been observed via in situ measurements (Brandt et al., 2002), SAR imagery
87 (Magalhães et al., 2016), MODIS (De Macedo et al., 2023), and SWOT data (Goret et al., 2026). This makes the
88 region an ideal laboratory for studying the tidal variability of IT responses during the propagation of tidal flux.
89 Using numerical modeling, Tchilibou et al. (2022) reported that the M2 coherent baroclinic tidal flux propagates
90 more northward during MAMJJ in the region off the Amazon shelf. During ASOND, however, it becomes
91 incoherent—branching and deviating near 6°N—due to strong interactions with MEs and background currents off
92 the Amazon shelf. This variability in flux behavior (e.g., free propagation, refraction, branching) during ASOND
93 may result from the interaction of the coherent flux with MEs, sheared currents (e.g., NECC), changes in
94 stratification, topography (e.g., Ceará Rise seamount, Mid-Atlantic ridge; Fig. 1), other internal wave sources, or
95 coupled processes.

96 Motivated by the complex mesoscale interplay off the Amazon shelf, we investigate the fate of IT within this
97 dynamic environment at daily timescales from the realistic model outputs. Specifically, we examine whether ITs
98 propagate freely, are deviated, or become trapped by mesoscale features. We further determine whether these
99 outcomes depend on the vertical modes of ITs, or the location of the ME encounters together with its associated
100 background conditions (currents and stratification), distinguishing, for instance, between interactions at a CE core
101 versus its edge. Finally, we explore the synergistic roles of topography (e.g., Ceará Rise seamount) and CEs in
102 governing modal energy transfers.



103
 104 **Figure 1.** Internal tide generation and propagation, and regional circulation off the Amazon shelf. Key IT
 105 generation sites (A–F) are marked along the shelf break slope, with the three primary sites (A, B, D) highlighted
 106 in red. The associated M_2 baroclinic energy flux, represented by black arrows, is the 25-hour mean depth-
 107 integrated flux from the September–December (SOND) 2015 period. The schematic background circulation
 108 includes the North Brazil Current (NBC), its retroreflection (NBCR), North Equatorial Countercurrent (NECC), and
 109 Equatorial Undercurrent (EUC) (solid blue lines). Mesoscale eddies are indicated by cyclonic (CEs, red circles)
 110 and anticyclonic eddies (AEs, blue circles), the latter including the NBC Ring. Topography, from the NEMO-
 111 AMAZON36 model, is detailed with the 200 m and 2000 m isobaths (grey lines) and specific features outlined by
 112 their 3500 m isobath (Ceará Rise seamount: green contour; Mid-Atlantic ridge: magenta contour).

113 2 Methodology

114 2.1 High-resolution numerical model: AMAZON36

115 We use outputs from the Nucleus for European Modelling of the Ocean (NEMO) model v4.0.2 (Madec et al.,
 116 2019), specifically the AMAZON36 configuration (Assene et al., 2024). This high-resolution ($1/36^\circ$, ~ 3 km)
 117 model is designed for the western tropical Atlantic (54.7° W– 35.3° W, 5.5° S– 10° N) and features 75 vertical
 118 layers, with 23 levels in the upper 100 m. The 3 km horizontal resolution provides approximately 30–60, 20–28,
 119 and up to 17 grid points per wavelength for Mode-1, Mode-2, and Mode-3 M_2 IT in the Amazon region,
 120 corresponding to horizontal wavelengths of ~ 90 – 180 km, ~ 60 – 85 km, and up to ~ 50 km, respectively (Tchilibou
 121 et al., 2022). This resolution ensures that all three modes are well resolved and accurately represents the

122 topography critical to their generation and propagation from the Amazon shelf break (Assene et al., 2024). The
 123 latter detailed more about the AMAZON36 configuration parameters.

124 The model simulations span 11 years, from January 2005 to December 2015, and provides three-dimensional daily
 125 and hourly outputs. This dataset has previously been used to study IT interactions with background currents and
 126 stratification, as well as IT impact on the ocean thermal structure (Assene al., 2024; Kouogang et al., 2025).

127 For this study, we focus on the period from September to December (SOND) 2015, when stronger mean currents
 128 and EKE contribute to more incoherent ITs (Tchilibou et al., 2022). To analyze the rapid variability of IT
 129 responses to MEs like CEs, we examine 25-hour segments, from hourly outputs, within the entire SOND season.

130

131 **2.2 Internal Tides and Mesoscale Activity**

132 Our analysis for each 25-hour window of AMAZON36 outputs during the SOND period involves several steps:
 133 extracting the M2 IT constituent, separating the barotropic and baroclinic components, projecting the baroclinic
 134 components onto vertical modes, extracting MEs and characterizing their properties, and examining the mean
 135 background current pattern and topographic features.

136

137 **2.2.1 Undecomposed IT Energy equations**

138 First, to examine the variability of IT responses to MEs, we explore all 25-hour snapshots of IT energy flux from
 139 the AMAZON36 output during the SOND period. Following the method of Kelly et al. (2010), barotropic and
 140 baroclinic tidal constituents were separated. This separation is performed directly by the NEMO model to ensure
 141 accuracy, providing the total energy for all resolved propagation modes at a given tidal frequency (Tchilibou et
 142 al., 2022). Our analysis focuses solely on the M2 harmonic, the dominant tidal constituent in this region (Gabioux
 143 et al., 2005; Fassoni-Andrade et al., 2023).

144 The energy budget for IT can be expressed from the following equations (Wang et al., 2016; Buijsman et al., 2012;
 145 Kerry et al., 2013; Tchilibou et al., 2022; Siyanbola et al. 2024):

146

$$147 \nabla_h \cdot \mathbf{F} + D + R = C \quad (1)$$

148

149 In contrast to energy budgets decomposed into vertical modes, we refer to these as the undecomposed IT energy
 150 equations. Here, $\nabla_h \cdot \mathbf{F}$ is the divergence of the depth-integrated energy flux, $\mathbf{F} = (F_x, F_y)$ the energy flux vector,
 151 C represents the depth-integrated barotropic-to-baroclinic energy conversion, and D is the depth-integrated energy
 152 dissipation term. The term R includes the energy tendency term, implicit horizontal dissipation, wave-mean flow
 153 and wave-wave interaction terms, and other offline computation errors. $\nabla_h = (\partial/\partial x, \partial/\partial y)$ is the horizontal gradient
 154 operator.

155 In the following, a particular attention is given to depth-integrated and time-averaged energy flux term \mathbf{F} , which
 156 was defined as (Tchilibou et al., 2022; Assene et al. 2024):

157

$$158 [\mathbf{F}_{bc}, \mathbf{F}_{bt}] = [\int_{-H}^{\eta} \mathbf{u}_{bc} p_{bc} dz, \mathbf{u}_{bt} p_{bt}], \quad (2)$$

159

160 where $\mathbf{u} = (u, v)$ is the horizontal baroclinic tidal velocity vector, and p the tidal pressure. Here, the subscripts bt
 161 and bc denote barotropic and baroclinic components, respectively. η is the sea surface height and H is the seafloor
 162 depth.

163

164 2.2.2 Projection of IT Motions Onto Vertical Modes

165 Second, to investigate whether the IT responses to MEs is mode-dependent and to examine potential inter-modal
 166 energy transfer, we project the M_2 tidal constituent onto a set of vertical modes for selected 25-hour snapshots
 167 that capture ME-induced IT responses. This selective approach substantially reduces the computational cost
 168 associated with processing high-resolution 3D data for all 25-hour windows during the SOND period.

169

170 Vertical Mode Decomposition

171 For each selected snapshot, we first extract the M_2 harmonic via harmonic analysis. Although performing
 172 harmonic fits over short (25-hour) segments may introduce frequency leakage from nearby tidal constituents (e.g.,
 173 S_2 , N_2 , and K_2) into the M_2 signal, this effect is expected to be small in our case because the tidal regime is
 174 strongly M_2 -dominated, accounting for more than 70% of the total tidal energy (e.g., Gabioux et al., 2005;
 175 Tchilibou et al., 2022; Fassoni-Andrade et al., 2023). This approach is consistent with previous studies that have
 176 successfully applied harmonic analysis to similarly short records to resolve semidiurnal constituents (e.g., 17–29
 177 h M_2 tidal observations in Waterhouse et al., 2018), demonstrating that dominant semidiurnal tides can be reliably
 178 estimated from short-duration data.

179 We then decompose the M_2 tidal currents and pressure using a locally computed set of vertical modes. This
 180 method provides a more accurate separation of barotropic and baroclinic tides than simpler approaches (Kelly,
 181 2016; Lahaye et al., 2020; Lahaye et al., 2024; Siyanbola et al. 2024).

182 The vertical modes are obtained by solving the standard Sturm-Liouville eigenvalue problem at each horizontal
 183 grid point, using the local mean stratification profile (based on the time-mean buoyancy frequency, $\overline{N^2}$), and
 184 assuming a flat bottom, a free surface, and no background flow (Gerkema and Zimmerman, 2008; Bella et al.,
 185 2024):

186

$$187 \partial_z \left(\frac{\partial_z \Phi_n}{N^2} \right) + \frac{\Phi_n}{c_n^2} = 0, \quad (3)$$

188

189 with the boundary conditions:

$$190 \partial_z \Phi_n = 0 \text{ at } z = -H, \text{ and } g \partial_z \Phi_n + \overline{N^2} \Phi_n = 0 \text{ at } z = \bar{\eta}, \quad (4)$$

191

192 where ∂_z denotes the partial derivative in z -direction, Φ_n is the horizontal velocity/pressure eigenfunction for
 193 mode n , c_n is the modal phase speed and g is the acceleration due to the gravity. The associated vertical
 194 velocity/buoyancy eigenfunction, φ_n , is given by:

195

$$196 \partial_z \varphi_n = \Phi_n, \text{ and } \partial_z \Phi_n = -\frac{\overline{N^2}}{c_n^2} \varphi_n. \quad (5)$$

197 It should be noted that the flat-bottom assumption could represent a limitation for higher-mode projections near
 198 steep topography such as the Ceara Rise seamount. The errors associated with this approximation are expected to
 199 be of a few percent for the dominant low modes (Kelly, 2016).

200 The vertical modes satisfy the orthogonality condition (Kelly, 2016; Lahaye et al., 2024; Bella et al., 2024):

201

$$202 \int_{-H}^{\bar{\eta}} \Phi_m \Phi_n dz = H \delta_{mn}, \quad (6)$$

203

204 where δ_{mn} is the Kronecker delta and $\bar{\eta}$ is the time-averaged sea surface height.

205 We solved Equation 3 for the first 11 modes ($n = 0, 1, \dots, 10$) at each grid point, where $n = 0$ represents the
 206 barotropic mode. In this study, the analysis of energy flux focuses primarily on the first three baroclinic modes
 207 ($n = 1, 2, 3$), which are the most dynamically significant at the model’s resolution (~ 3 km). These three baroclinic
 208 modes account for 96.2% (33.2%), 96.8% (37.9%), and 97.2% (26.3%) of the total baroclinic energy flux (relative
 209 to the combined baroclinic and barotropic flux) in the NE, CEC, and CEE cases, respectively. They therefore
 210 capture the dominant share of the baroclinic energy, supporting their use as the basis of our analysis.

211 The horizontal velocity \mathbf{u} and pressure p fields are projected onto these modes to obtain the depth-independent
 212 modal amplitudes:

213

$$214 [\mathbf{u}_n(\mathbf{x}, t), p_n(\mathbf{x}, t)] = \frac{1}{H} \int_{-H}^{\bar{\eta}} [\mathbf{u}(\mathbf{x}, z, t), p(\mathbf{x}, z, t)] \Phi_n(\mathbf{x}, z) dz, \quad (7)$$

215

216 with $\mathbf{x} = (x, y)$ denoting the horizontal direction.

217 The full 3D structure of \mathbf{u}_n fields for each mode can be reconstructed as (Li et al., 2024):

218

$$219 \mathbf{u}_n(\mathbf{x}, z, t) = \mathbf{u}_n(\mathbf{x}, t) \Phi_n(\mathbf{x}, z) \quad (8)$$

220

221 Modal Energy Budget

222 To analyze the inter-modal energy transfer/scattering and redistribution, we examine the terms of the modal
 223 energy budget of a given mode interacting with physical features such as topography and mesoscale flow (Fan et
 224 al., 2024; Bella et al., 2024; Kelly, 2016; Kelly and Lermusiaux, 2016):

$$225 \nabla_h \cdot \mathbf{F}_m + D_m + \Psi_m = \sum_n (C_{mn} + A_{mn} + H_{mn} + V_{mn} + B_{mn}). \quad (9)$$

226 Here:

- 227 • C_{mn} is the nonlinear scattering (from mode $m > 0$ into mode n) of energy by topography and stratification.
- 228 • A_{mn} represents the advection of the ITs by the background flow and MEs.
- 229 • H_{mn} and V_{mn} represent the effect of the horizontal and vertical shear of the background flow, respectively.
- 230 • $\mathbf{F}_m = H p_m \mathbf{u}_m$ is the depth-integrated and time-averaged baroclinic energy flux for mode n .
- 231 • B_{mn} consist of the three-way interaction term and the horizontal gradient of the buoyancy field.
- 232 • Ψ_m consists of the energy tendency terms.

233 • D_m is the dissipation term of modal energy budget, which also includes interactions with unresolved modes,
 234 other physical dissipation processes leading to local dissipation (Alford & Zhao, 2007), and other offline
 235 computation errors.

236 A previous seasonal-scale study by Bella et al. (2024) found the nonlinear coupling terms C_{mn} , A_{mn} , H_{mn} , and
 237 V_{mn} to be dominant across the North Atlantic basin. For our investigation on a daily timescale, a preliminary
 238 analysis identified C_{mn} and H_{mn} as the dominant terms in our study region. We therefore focus on estimating
 239 these dominant couplings terms as defined by Bella et al. (2024):

240

$$241 \quad C_{mn} = \langle H p_m \mathbf{u}_n \cdot T_{nm} - H p_n T_{mn} \cdot \mathbf{u}_m \rangle, \quad (10)$$

242

$$243 \quad H_{mn} = \langle -H (U_{mn}^h \mathbf{u}_n) \cdot \mathbf{u}_m \rangle, \quad (11)$$

$$244 \quad \text{With } T_{mn} = \frac{1}{H} \int_{-H}^{\bar{\eta}} \Phi_m \nabla_h (\Phi_n) dz, \quad (U_{mn}^h)_{ij} = \frac{1}{H} \int_{-H}^{\bar{\eta}} \Phi_m \Phi_n \frac{\partial \bar{U}_{h,i}}{\partial x_j} dz.$$

245

246 Here, the angle bracket $\langle \cdot \rangle$ denotes the average over a M2 tidal period, $\bar{U}_h = (\bar{U}, \bar{V})$ is the time-averaged total
 247 horizontal velocity vector. $\frac{\partial \bar{U}_{h,i}}{\partial x_j}$ is the tensor.

248 The modal horizontal kinetic energy (HKE_n) of M2 IT is estimated as (Kelly et al., 2012; Fan et al., 2024):

249

$$250 \quad HKE_n = \frac{\rho_0 H}{2} \langle u_n^2 + v_n^2 \rangle, \quad (12)$$

251 where ρ_0 is the reference density.

252

253 **Symmetric–Antisymmetric Separation of Nonlinear Coupling Terms**

254 The energy transfer matrices—including topographic scattering (C_{mn}) and (H_{mn})—are decomposed into
 255 symmetric and antisymmetric components, following the established methodology (Savage et al., 2020; Bella et
 256 al., 2024). For any general transfer matrix (X_{mn}), the standard mathematical definitions are: the antisymmetric
 257 component, $X_{mn}^A = \frac{1}{2} (X_{mn} - X_{nm})$, and the symmetric component, $X_{mn}^S = \frac{1}{2} (X_{mn} + X_{nm})$.

258 The antisymmetric component, X_{mn}^A , represents the internal reallocation of energy—specifically, the scattering
 259 or transfer of energy among the various IT vertical modes. Critically, this process conserves the total energy of
 260 the IT field, as it analytically redistributes energy across the system modes and spatial scales without introducing
 261 a net gain or loss. For instance, the term C_{mn} is inherently antisymmetric and thus provides a canonical reference
 262 for conservative internal energy transfer.

263 Conversely, the symmetric component, X_{mn}^S , describes the net energy exchange between the IT and the low-
 264 frequency background flow. When integrated in a basin, this component acts as a source or sink for the IT system,
 265 quantifying the total energy gained from or lost to the slowly varying circulation (Bella et al., 2024).

266 The direction of energy transfer is interpreted from the sign of the matrix elements. Considering a specific mode
 267 m:

268 • For the full matrix X_{mn} , a negative value indicates a net forward transfer of energy from mode m to mode n,
 269 while a positive value indicates a net backward transfer from mode n to mode m;

- For the antisymmetric component X_{mn}^A , a negative value signifies a forward transfer from mode m to mode n of the IT field, and a positive value signifies a backward transfer;
- For the symmetric component X_{mn}^S , a negative value indicates a forward transfer from mode- m IT to the mode- n background flow, whereas a positive value indicates energy is transferred from the mode- n background flow to mode- m IT.

275

276 2.2.3 Eddy detection and structure

277 Third, to investigate whether the IT responses to MEs depend on the eddy encounter location, including the
 278 associated background conditions (currents and stratification), we detected and characterized eddies from 25-hour
 279 mean snapshots of AMAZON36 output during the SOND period.

280 The mesoscale activity in this region during the 2015 ASOND period was previously assessed by Tchilibou et al.
 281 (2022). Their analysis, which compared the model's surface EKE with satellite data, showed reasonable agreement
 282 in both the spatial pattern and amplitude of the mean EKE, especially in regions dominated by the NECC.

283 Eddies were identified in our model outputs using the Okubo-Weiss parameter (W), chosen for its ability to detect
 284 coherent vortices on specific isopycnal surfaces or depths (Okubo, 1970; Weiss, 1991; Kurian et al., 2011; Xu et
 285 al. 2019). The W parameter is defined as:

286

$$287 W = S_n^2 + S_s^2 - \zeta^2, \quad (13)$$

288

289 where the normal strain (S_n) and shear strain (S_s), and the relative vorticity (ζ) are:

290

$$291 S_n = \frac{\partial u}{\partial x} - \frac{\partial v}{\partial y}, \quad S_s = \frac{\partial v}{\partial x} + \frac{\partial u}{\partial y}, \quad \zeta = \frac{\partial v}{\partial x} - \frac{\partial u}{\partial y}. \quad (14)$$

292

293 Regions where rotation ($W < 0$) dominates over strain ($W > 0$) indicate potential eddy cores.

294 The detection of eddies on selected isopycnal surfaces (between 23 and 27 kg m^{-3} isopycnals) following the
 295 procedure of Kurian et al. (2011) and Xu et al. (2019). First, the W fields were smoothed using a 50 km \times 50 km
 296 half-power filter to suppress small-scale noise. For each 25-hour mean snapshot, we then applied a constant
 297 threshold of $W_0 = -3 \times 10^{-11} \text{ s}^{-2}$ to isolate vorticity-dominated regions ($W < W_0$). Closed contours corresponding
 298 to $W = W_0$ were identified, and each contour was subjected to a series of quality control criteria to be classified
 299 as an eddy: a shape error (deviation from a fitted circle) of less than 50%, a mean azimuthal velocity greater than
 300 5 cm s^{-1} , and a radius larger than 50 km.

301 For each identified eddy, its thickness was defined as the vertical extent of its W_0 contours, and its center location
 302 was defined as the centroid of the closed W_0 contour. Detected eddies were classified as cyclonic or anticyclonic
 303 based on the sign of their potential vorticity anomaly (PVA, positive for CEs and negative for AEs; Fig. 2a).

304

305 To analyze the eddy dynamical structure, we used the framework of rescaled potential vorticity (PV_r). This method
 306 filters out high-frequency wave noise to isolate the balanced mesoscale signal. The PV_r is derived from the
 307 classical Ertel (1942) potential vorticity, rescaled by a reference stratification at rest, $\rho^*(z)$, following the approach
 308 of Morel et al. (2023, 2019) and subsequent studies (e.g., Delpech et al., 2020; Aguedjou et al., 2021; Ernst et al.,
 309 2023).

310 Its expression is:

311

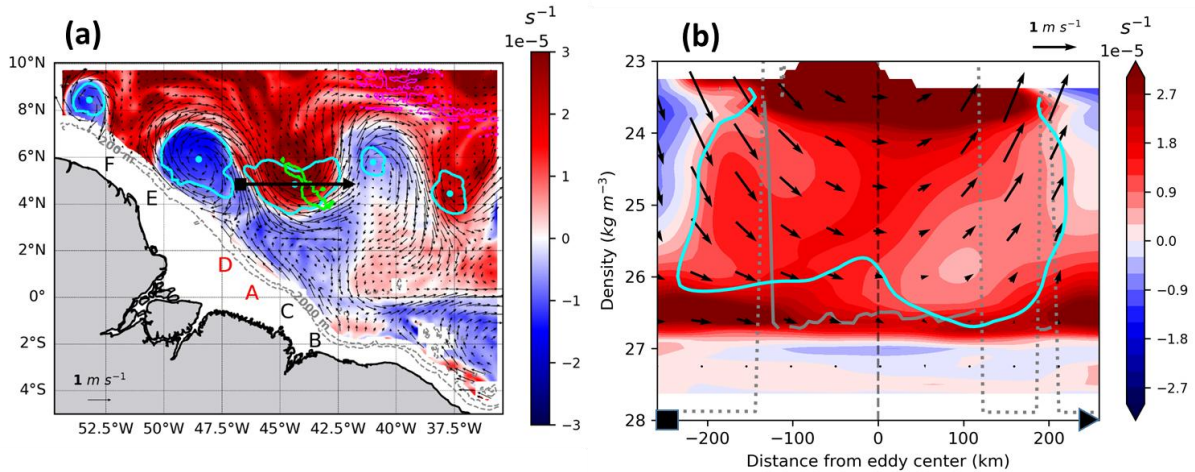
$$312 \quad PV_r = (\nabla \times \mathbf{U} + f) \cdot \nabla \mathbf{Z}(\rho) = \nabla \cdot [(\nabla \times \mathbf{U} + f) \mathbf{Z}(\rho)], \quad (15)$$

313

314 where $\mathbf{U} = (\bar{U}, \bar{V}, \bar{W})$ is the time-mean total velocity vector, and f is the local Coriolis parameter. $\mathbf{Z}(\rho)$ is a rescaling
 315 function of time-mean potential density ρ , defined using the reference density profile ρ^* so that $\mathbf{Z}(\rho^*(z)) = z$. ρ^*
 316 is defined by the adiabatically rearranged state of minimum potential energy, following the concept of Lorenz
 317 (1955) as formalized by Nakamura (1995) and Winters and D'Asaro (1996). An eddy dynamical core is then
 318 identified by its anomaly from the background planetary vorticity, $PVA = PV_r - f$, within a layer bounded by two
 319 isopycnals.

320

321 To distinguish subsurface eddies from surface-intensified ones, we classified them based on the isopycnal level
 322 of their core of PVA. Following the method of Kouogang et al. (2025), we used the base of the pycnocline (defined
 323 by $\sim 26.5 \text{ kg m}^{-3}$ isopycnal) as the boundary of the lower pycnocline depth. Eddies with their PVA core on
 324 isopycnals less dense than 26 kg m^{-3} were classified as surface-intensified eddies (Fig. 2b), while those with their
 325 core on denser isopycnals ($> 26.5 \text{ kg m}^{-3}$) were classified as subsurface-intensified eddies as formalized by
 326 Aguedjou et al. (2021) in the tropical Atlantic Ocean. This classification scheme was applied to all eddies detected
 327 during the SOND period. This study focuses specifically on these surface-intensified eddies.



328

329 **Figure 2.** Detection and vertical structure of a representative ME (17 September 2015). (a) PVA (color shading)
 330 averaged within the $23\text{--}25.5 \text{ kg m}^{-3}$ isopycnal layer ($\sim 50\text{--}160 \text{ m}$ depth). Panel (a) shows detected eddy edges
 331 (cyan contours), eddy centroids (cyan dots), and mean background currents (black arrows) along the 24 kg m^{-3}
 332 isopycnal. (b) Vertical cross-section of PVA along the transect in (a) (black arrow), passing through the core of a
 333 CE. The transect endpoints are marked by a square (start) and triangle (end). The vertical dashed black line
 334 indicates the eddy centroid, black arrows show the CE-associated currents, and grey lines mark the upper (dotted)
 335 and lower (solid) thermocline limits. PVA and mean background currents fields were smoothed using a $50 \text{ km} \times$
 336 50 km half-power filter to suppress small-scale noise. Topography is detailed with the 200 m and 2000 m isobaths
 337 (grey lines) and specific features outlined by their 3500 m isobath (Ceará Rise seamount: green contour; Mid-
 338 Atlantic ridge: magenta contour).

339

340 3 Results

341 In order to examine the variability of IT responses to MEs, particularly to CEs, we first present three representative
342 cases of interactions between the (non-modal) baroclinic energy flux of the M2 IT and the detected eddy fields,
343 identified from all 25-hour mean snapshots during SOND 2015. We then analyze the IT's vertical mode responses,
344 focusing on the encounter location of the fluxes — originating from the most energetic generation sites A and D
345 — with a CE along their path, and examine the potential modal energy transfer and redistribution.

347 3.1 Variability of IT responses to MEs: three distinct cases

348
349 Following the method described in Sects. 2.2.1 and 2.2.3 (Eqs. (1)-(2) and (13)-(15)), we identified three distinct
350 cases from the SOND 2015 period for analysis, each occurring near a spring tide maximum to ensure comparably
351 high tidal energy levels (Fig. 3). This setup minimizes the influence of tidal variability, allowing us to isolate the
352 eddy-induced effects. Although the tidal forcing is not strictly identical across the three cases, the differences in
353 tidal amplitude remain small (less than 18%) and are therefore considered secondary compared to the large
354 contrasts in mesoscale conditions between the cases.

355 Figure 4 illustrates in the three relevant cases, the M_2 baroclinic energy flux, and MEs detected and their polarity
356 given by the sign of PVA. The three selected cases are located in a region shaped by two major topographic
357 features: the Ceara Rise seamount (~500 km from sites A and D; between 4°N–6°N, 45°W–42.5°W), with an
358 amplitude (h_{\max}) of ~1000 m and a width (w_{\max}) of ~100 km, and the Mid-Atlantic Ridge (~1100 km from sites A
359 and D). Each case was selected to highlight distinct IT responses:

- 360 • No-Eddy case (NE, 24 November 2015): Energy flux from the primary generation sites (A and D) propagated
361 freely, crossing the seamount and reaching the ridge. A similar pattern was observed from site B (Fig. 4a);
- 362 • Cyclone Eddy Center case (CEC, 17 September 2015): Energy flux from sites A and D was refracted into a
363 single beam at the core of a CE positioned (4.9° N, 44.4° W) above the seamount. Separately, flux from the
364 less energetic site E was also refracted into a single beam, emanating from the center of a nearby AE (centered
365 at 5.9° N, 48.5° W) (Fig. 4b);
- 366 • Cyclone Eddy Edge case (CEE, 29 September 2015): Energy flux from sites A and D was diffracted into
367 multiple beams at the eastern edge of a CE located (5.3° N, 45.0° W) on the northern flank of the seamount
368 (Fig. 4c).

369 Across the three selected cases, the analysis of the background conditions (stratification and currents) along a
370 transect following the IT paths from sites A and D reveals strong background currents ($>1.0 \text{ m s}^{-1}$, Fig. 5). In the
371 NE case (Figs. 5a,d), these currents are dominated by their cross-transect component (Fig. 5a), associated with
372 the NBC near the Amazon shelf-break and with the NECC near the seamount. In the eddy cases, the background
373 currents at the CE encounter location differs between cases: in the CEC case (Figs. 5b,e), the currents have both
374 cross- and along-transect components, whereas in the CEE case (Figs. 5c,f), they are dominated by their along-
375 transect component (Fig. 5f). In both eddy cases, the currents at the CE encounter location are associated with the
376 coupled NECC/CE flow. Away from the CE encounter location and the seamount, the background currents exhibit
377 a strong along-transect component associated with the NECC coupled with circulation from a nearby small AE.
378 Regarding background stratification, the horizontal gradient of the mean buoyancy frequency ($\nabla \overline{N^2}$, Appendix
379 A, Fig. A1) along the IT paths from sites A and D shows strong signatures ($O(10^{-8} \text{ m}^{-1} \text{ s}^{-2})$) localized near

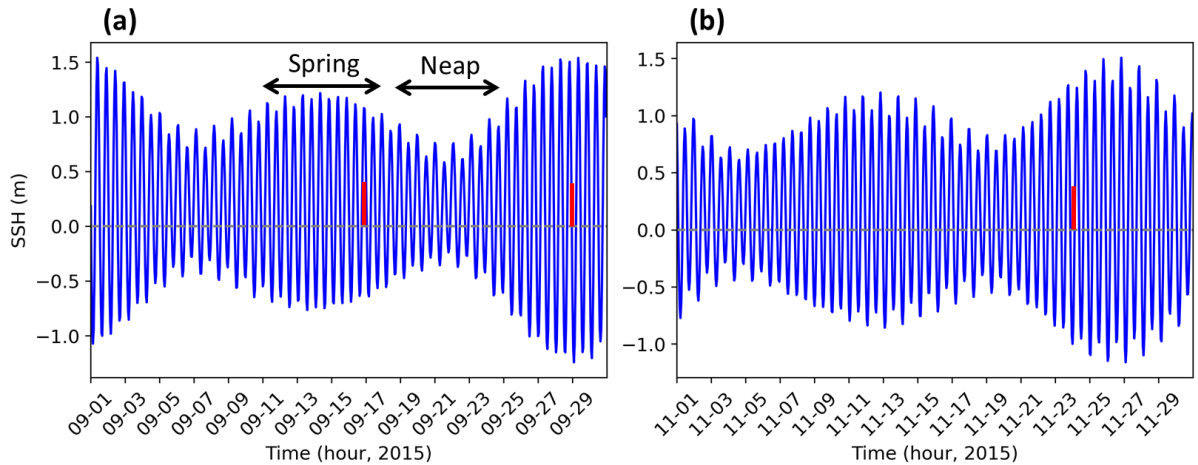
380 topographic features (seamount and ridges). At the CE encounter and seamount locations in the eddy cases, the
 381 horizontal stratification gradient is also similarly strong, except in the CEC case where it is quasi-uniform
 382 (Appendix A, Fig. A1). The strong background stratification is associated with the NECC in the NE case and with
 383 the coupled NECC/CE in the CEC case. Overall, the key distinction between the eddy cases lies not only in where
 384 the IT beam encounters the eddy (eddy core vs. eddy edge), but also in the associated background conditions
 385 (currents and stratification).

386 It should be noted that the eddy core/center and eddy edge are defined as regions where $r/R \approx 0$ and $r/R \approx 1$,
 387 respectively, where r is the distance from the eddy centroid and R is the radius of maximum velocity. This
 388 geometric difference in the CE encounter location leads to markedly different energetic behavior, as discussed
 389 below.

390 In this study, the three cases are qualitatively distinguished by the presence or absence of a CE, and, when a CE
 391 is present, by the geometry of the IT–CE intersection.

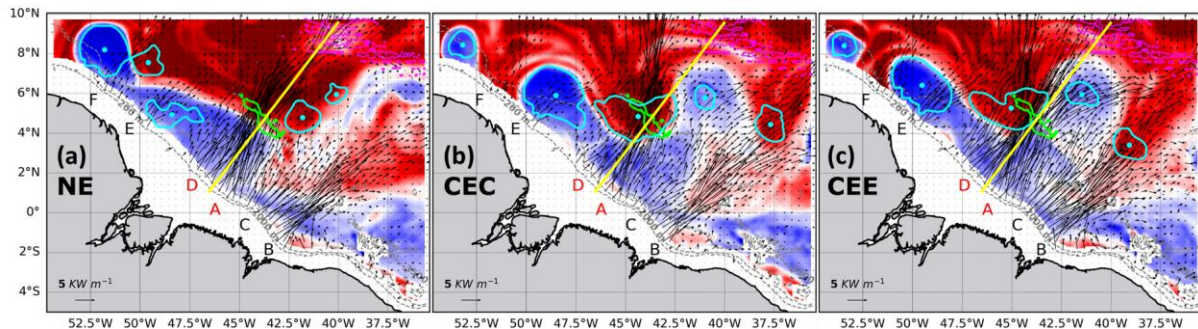
392

393 To determine whether the IT response patterns depend on the IT's vertical structure or on the eddy encounter
 394 location, we focus on the IT response to CEs and project the energy flux into vertical modes (Sect. 2.2.2). This
 395 approach enables us to examine the specific response of each vertical mode to the CE and potential modal energy
 396 redistribution and transfer resulting from these interactions.



397

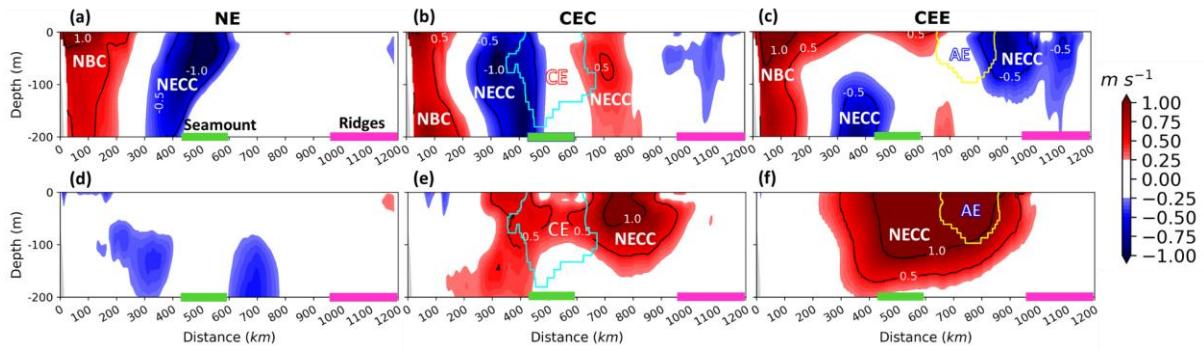
398 **Figure 3.** Sea surface height (SSH) from AMAZON36 simulations (station location: 1.29° N, 46.34° W) in (a)
 399 September and (b) November 2015. Red bars denote the three case study dates, and black arrows mark the spring-
 400 neap tidal cycle.



401

402 **Figure 4.** Depth-integrated M2 total baroclinic energy flux (black arrows) and isopycnally-averaged PVA (color
 403 shading), for the (a) NE, (b) CEC, and (c) CEE cases. All fields are 25-hour mean snapshots. The PVA is averaged

404 within the 23–25.5 kg m⁻³ density layer (approximately 50–160 m). Detected eddies along the 24 kg m⁻³ isopycnal
 405 are overlaid, with edges (cyan contours) and centroids (cyan dots). The respective dates are 24 November 2015
 406 (a), 17 September 2015 (b), and 29 September 2015 (c). The transects (yellow lines) highlight the most energetic
 407 energy flux pathways considered, originating from sites A and D. These transects are identical across all three
 408 cases to facilitate direct comparison. Topography is detailed with the 200 m and 2000 m isobaths (grey lines) and
 409 specific features outlined by their 3500 m isobath (Ceará Rise seamount: green contour; Mid-Atlantic ridge:
 410 magenta contour).



411
 412 **Figure 5.** Vertical structure of the mean background current velocity in the upper 200 m, shown along transects
 413 defined on the IT propagation paths from sites A and D (Fig. 4). The cross-transect (panels a–c) and along-transect
 414 (panels d–f) components of current velocity are shown for the NE (a, d), CEC (b, e), and CEE (c, f) cases. In
 415 panels (a–c), positive (negative) values indicate flow oriented approximately northwestward (southeastward). In
 416 panels (d–f), positive (negative) values indicate flow oriented approximately northeastward (southwestward).
 417 Notable topographic features are outlined by colored rectangles (seamount: green; ridges: magenta). Panels (b),
 418 (c), (e), and (f) also show the detected eddy edges for AE (yellow) and CE (cyan).

419 3.2 IT Responses to CEs

420 Following the method described in Sect. 2.2.2 (Eqs. (3)-(12)), we separately analyze the first three vertical modes
 421 of the M2 IT in the three cases.

422 3.2.1 NE Case: IT without Eddy

423 We first analyse the tidal energy diagnostics for the NE case to establish an eddy-free propagation baseline.
 424 Figures 6a-c maps the energy flux propagation and HKE for the first three modes, revealing distinct patterns for
 425 each one.

426 Mode-1 energy propagation is highly dominant. The fluxes, generated from sites A and D, constructively form a
 427 notably coherent beam that converges and propagates northeastward (~37° azimuth) for over 1100 km with
 428 minimal deviation (Fig. 6a). This long-distance propagation maintains a relatively constant HKE of 150–200 J
 429 m⁻², with a wavelength (λ_1) estimated between 90–125 km. In contrast, the Mode-2 flux propagates a significantly
 430 shorter distance (500–600 km, λ_2 : 60–85 km) and terminates abruptly at the seamount (Fig. 6b). Mode-3 forms no
 431 coherent beams but appears as scattered patches extending only 50–100 km (λ_3 : 35–50 km; Fig. 6c). Along their
 432 respective beams, Mode-1 and Mode-2 exhibit stronger energy flux amplitudes (>200 W m⁻¹) compared to Mode-
 433 3.

437 3 ($<200 \text{ W m}^{-1}$). The spatial distribution of these modal energy fluxes is consistent with the vertical structure of
438 the corresponding baroclinic velocity profiles (Appendix B, Figs. B1–B2). A sharp Mode-2 damping is clearly
439 visible over the seamount, while Mode-3 energy appears trapped over the seamount and ridge where the Mode-1
440 flux diminishes, suggesting that topographic features drive scattering to higher vertical modes.

441

442 To quantitatively assess the mechanisms responsible for this energy loss, we compute intermodal energy transfer
443 terms (Eqs. (9)-(11)) and map only the dominant terms in Figures 5d-o. These dominant terms, of order of
444 magnitude comparable ($O(10^{-8} \text{ W m kg}^{-1})$), are topographic scattering term (C_{mn} , Eq. (10)), and the horizontal
445 shear term (H_{mn} , Eq. (11)) of background flow. They then are separated into its antisymmetric and symmetric part
446 for the analysis. All other background flow-induced energy transfer terms, such as advection and vertical shear,
447 are negligible in comparison ($O(10^{-10} \text{ W m kg}^{-1})$; figures not shown).

448

449 The analysis reveals a primary pathway of intermodal energy transfer driven by topographic scattering term (C_{mn}),
450 which is antisymmetric by construction. Along the IT path from generation sites A and D, a dominant forward
451 energy cascade ($|C_{mn}| \sim 4 \times 10^{-8} \text{ W m kg}^{-1}$) occurs near major bathymetric features—the shelf break and seamount.
452 Specifically, energy is sequentially transferred from Mode-1 to Mode-2 IT for C_{12} (Fig. 6e, blue patches), and
453 then from Mode-2 to Mode-3 IT for C_{23} (Figs. 6f, blue patches). For C_{13} , however, energy exchanges between
454 Mode-1 and Mode-3 IT are bidirectional—energy is both lost and gained—and spatially confined to the vicinity
455 of topographic features (Fig. 6d, blue and red patches). This could stem from the background conditions,
456 particularly the notable effect of the horizontal stratification gradient in the coupling term C_{mn} (Appendix A, Fig.
457 A1), or the influence of shear in the background flow (NBC, NECC), the effect of which is discussed in detail
458 below.

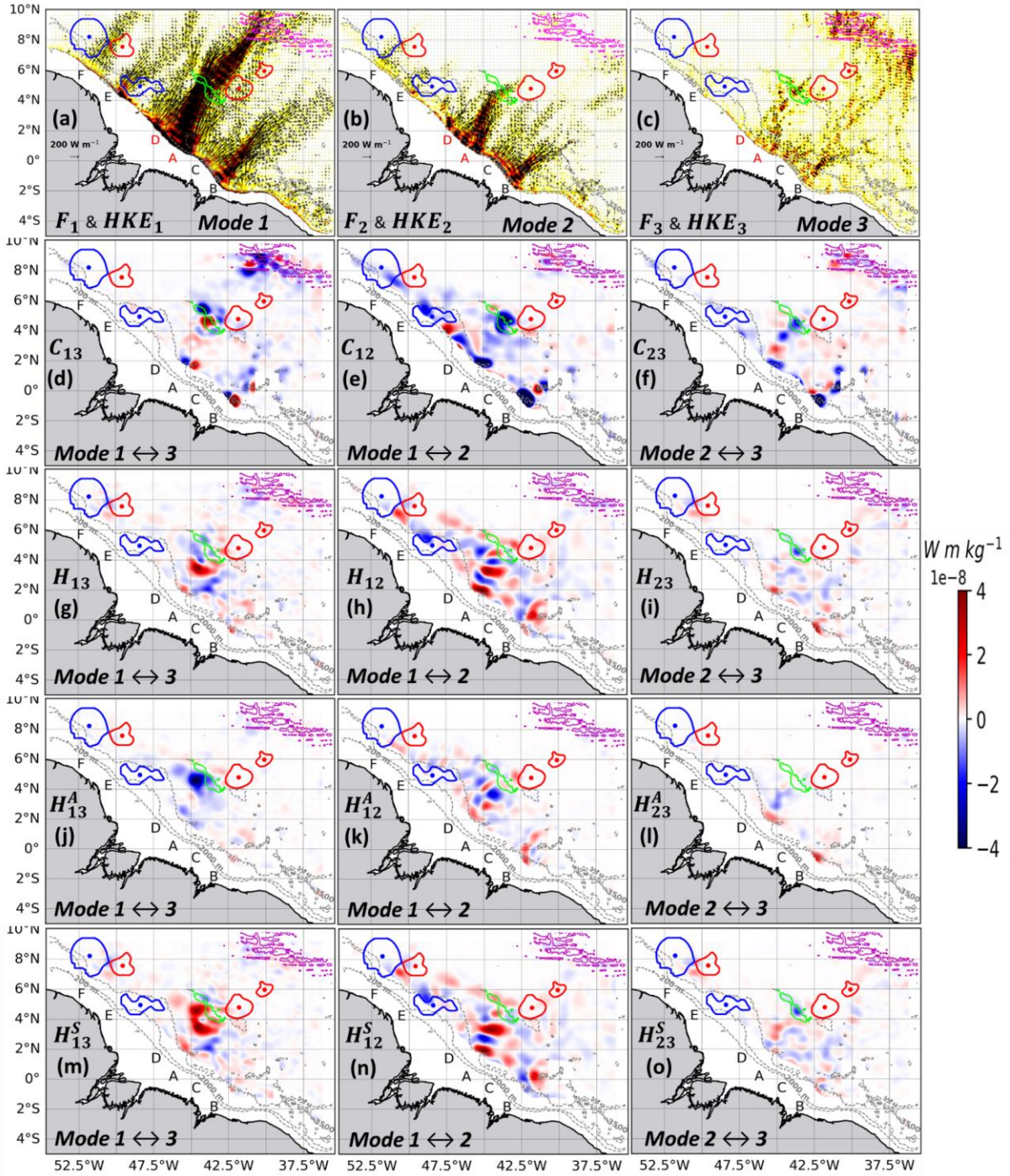
459

460 Decomposing the horizontal shear term H_{mn} (Figs. 6g–i) into its antisymmetric (Figs. 6j–l) and symmetric (Figs.
461 6m–o) components shows that its net influence ($|H_{mn}| \sim 4 \times 10^{-8} \text{ W m}^{-1} \text{ kg}^{-1}$) is more due to the symmetric part.
462 This latter facilitates energy exchanges between the background flow and the IT modes along the IT path from
463 the most energetic sites. Indeed, before the seamount, the symmetric terms H_{12}^S and H_{13}^S are both strongly
464 dominant in their net effect, while H_{23}^S is weakly dominant in H_{23} . In this region, energy is strongly transferred
465 from the Mode-2 and Mode-3 background flow to the Mode-1 IT (Figs. 6m,n, red patches). Over the seamount,
466 the symmetric part of H_{mn} becomes notable. Here, energy transfers are weak overall, but a notable transfer occurs
467 from the Mode-2 IT to the Mode-3 background flow (Fig. 6o, blue patches).

468

469 In essence, in the NE case, coherent energy flux from sites A and D converges and propagates until encountering
470 major topographic features (seamounts and ridges). While Mode-1 IT energy propagates over long distances with
471 amplitudes exceeding 200 W m^{-1} , the higher modes behave differently. Mode-2 IT energy, despite having a
472 comparable amplitude to Mode-1, is effectively damped. In contrast, the weaker Mode-3 IT energy ($<200 \text{ W m}^{-1}$)
473 becomes trapped by the topography. The interaction with topographic features, potentially enhanced by the
474 background flow, triggers significant intermodal energy transfer on the order of $10^{-8} \text{ W m}^{-1} \text{ kg}^{-1}$. This transfer is
475 governed by two primary mechanisms: 1) topographic scattering drives a dominant forward energy cascade

476 through the IT modes (Mode-1 \rightarrow Mode-2 \rightarrow Mode-3), and 2) the horizontal shear of the background flow
 477 facilitates a direct energy scattering from the Mode-2 and Mode-3 background flow to Mode-1 IT.



478
 479 **Figure 6.** Tidal energy diagnostics for the NE case on 24 November 2015, averaged over a M2 tidal period. Panels
 480 (a–c) show the depth-integrated M2 baroclinic energy fluxes (F_m ; black arrows) and horizontal kinetic energy
 481 (HKE_m ; color shading) for (a) mode-1 (F_1 , HKE_1), (b) mode-2 (F_2 , HKE_2), and (c) mode-3 (F_3 , HKE_3). Panels
 482 (d–f) present the effects of topographic scattering and stratification (C_{mn} ; color shading) for (d) C_{13} , (e) C_{12} , and
 483 (f) C_{23} . Panels (g–i) show the net component of horizontal shear induced by the mean background flow (H_{mn} ; color
 484 shading) for (g) H_{13} , (h) H_{12} , and (i) H_{23} . Panels (j–l) show the antisymmetric component of this horizontal shear
 485 (H_{mn}^A ; color shading) for (j) H_{13}^A , (k) H_{12}^A , and (l) H_{23}^A . Panels (m–o) show the symmetric component of horizontal
 486 shear (H_{mn}^S ; color shading) for (m) H_{13}^S , (n) H_{12}^S , and (o) H_{23}^S . All panels include the detected eddy edges (closed

487 contours) and eddy centroids (dots) for anticyclones (blue) and cyclones (red). Topography is shown using
488 200 m and 2000 m isobaths (grey contours), with specific features highlighted by the 3500 m isobath (seamount:
489 green contour; Mid-Atlantic Ridges: magenta contour). The C_{mn} and H_{mn} fields were smoothed with a Gaussian
490 filter ($\sigma = 7$ grid points) to aid interpretation. It should be noted that the colorbar range is saturated in panels to
491 enhance the visibility of energy transfer features.

492

493 3.2.2 CEC Case: IT Encountering a CE Core

494

495 We next examine IT responses when the energy flux from sites A and D encounter the core of a surface-intensified
496 CE (CEC case, Fig. 2b). The CE, centered at 4.9° N, 44.4° W above the localized mid-seamount, has a radius of
497 157 km, maximum velocity 1.35 m s^{-1} , and a core bounded by $23\text{--}25.5 \text{ kg m}^{-3}$ isopycnals extending $\sim 150 \text{ m}$
498 within the pycnocline.

499

500 Prior to interaction, the incident mode-1 IT energy fluxes converge and interfere. Upon encountering the CE core,
501 this energy is refracted into a single beam (Fig. 7a), which emanates from the eddy center and propagates
502 northward at approximately 35° from their northeastward incident direction. Both incident and refracted beams
503 maintain comparable HKE of $150\text{--}200 \text{ J m}^{-2}$ (Fig. 7a), though the refraction process locally confines the energy,
504 leading to a reduction in HKE ($25\text{--}50 \text{ J m}^{-2}$) in the northwestern lee of the eddy. Concurrently, the Mode-2 IT
505 energy flux is blocked at the southern edge of the CE and seamount (Fig. 7b), while Mode-3 appears as scattered
506 patches in the regions where Mode-2 is trapped (Fig. 7c), indicating active intermodal energy scattering. As in the
507 NE case, Mode-1 and Mode-2 IT exhibit higher energy flux amplitudes ($>200 \text{ W m}^{-1}$) along their beams than
508 Mode-3 ($<200 \text{ W m}^{-1}$) (Figs. 7a-c). The vertical structure of the along-transect baroclinic velocity further supports
509 these results (Appendix B, Figs. B1, B3).

510

511 An analysis parallel to that conducted for the NE case identified the topographic scattering term (C_{mn}) and the
512 horizontal shear term (H_{mn}) of the background flow as the dominant mechanisms responsible for the active energy
513 scattering observed.

514

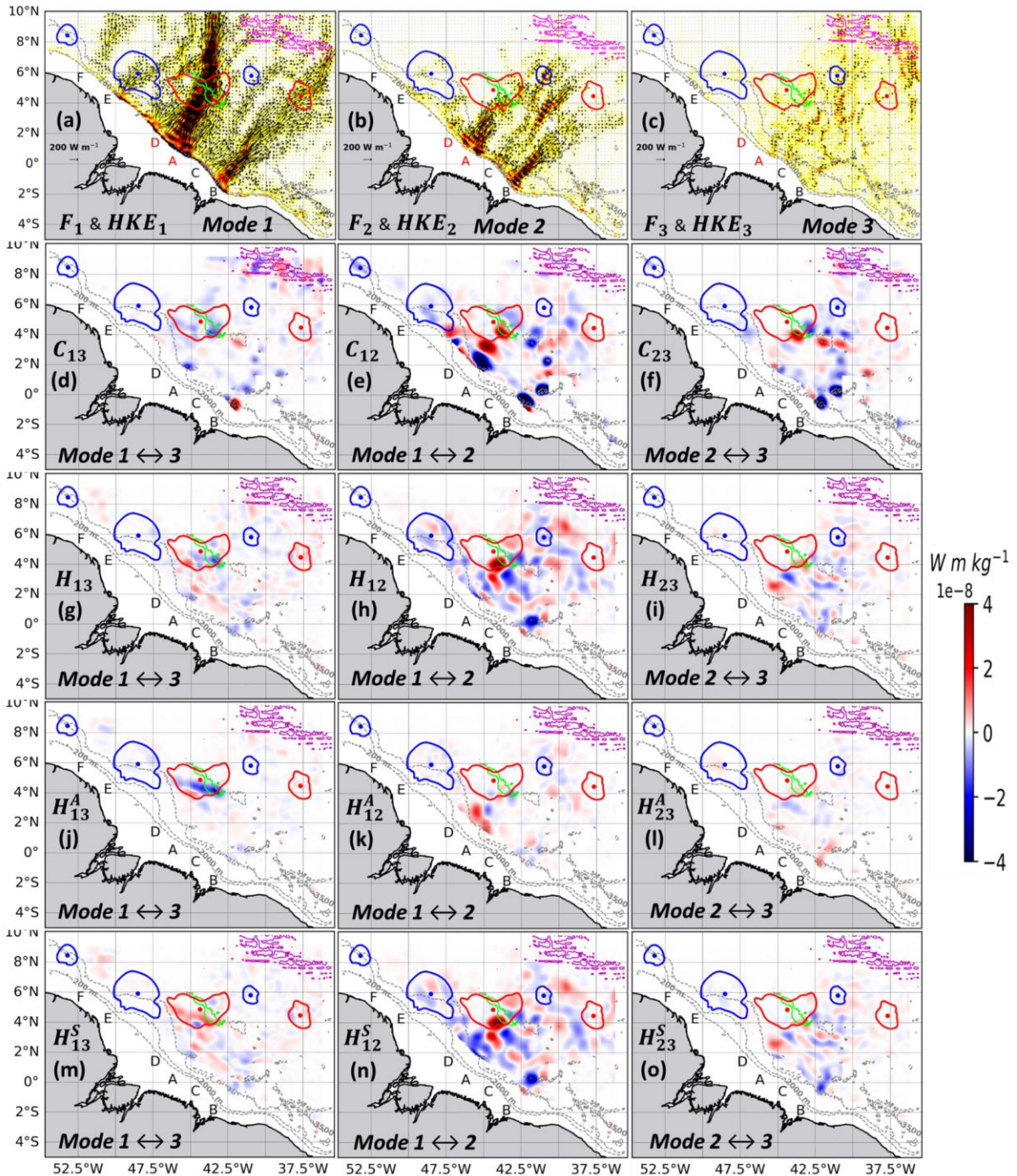
515 The analysis of the term C_{mn} in the CEC case reveals a distinct coupling pattern modulated by the CE core in
516 conjunction with the seamount along the IT path from sites A and D. A dominant forward energy transfer ($|C_{mn}|$
517 $\sim 4 \times 10^{-8} \text{ W m kg}^{-1}$) from Mode-1 to Mode-2 occurs near the shelf break for C_{12} (Fig. 7e, blue patches), consistent
518 with the NE case (Fig. 6e). A significant shift occurs near the southern edge and core of the CE, where a dominant
519 backward energy transfer is observed (with the exception of Mode-1 to Mode-3 IT). Here, energy is sequentially
520 gained by Mode-1 from Mode-2 for C_{12} (Fig. 7e, red patches near the southern edge and core of the CE) and by
521 Mode-2 from Mode-3 for C_{23} (inverse cascade, Fig. 7f, red patches), while energy is simultaneously lost from
522 Mode-1 to Mode-3 for C_{13} (direct forward transfer, Fig. 7d, blue patches). These patterns could be due to either
523 the horizontal stratification gradient in the coupling term C_{mn} associated with the CE (Appendix A, Fig. A1), or
524 shear in the background flow (NECC/CE).

525

526 Analysis of the background flow horizontal shear term (H_{mn}) shows that its magnitude ($|H_{mn}| \sim 4 \times 10^{-8} \text{ W m}^{-1}$
527 kg^{-1}) is comparable to the topography scattering term as in NE case. In the CEC case, along the energy flux from
528 sites A and D, the net effect of H_{mn} (Figs. 7g-i) is primarily due to its symmetric part (Figs. 6m-o), except for term
529 H_{13} . Between the shelf break and the southern edge of the CE, both the symmetric terms H^S_{12} and H^S_{23} are both
530 strongly dominant in their net effect. In this region, energy is both lost and gained between the Mode-1 IT and the
531 Mode-2 background flow, and between the Mode-2 IT and the Mode-3 background flow (Figs. 7n,o, blue patches).
532 This bidirectional transfer is spatially confined to this region and more pronounced between the Mode-1 IT and
533 the Mode-2 background flow, a pattern also present in the NE case (Figs. 6h,n). Near the CE center and seamount,
534 the terms H^A_{13} and H^S_{13} weakly combine to form H_{13} (Fig. 7j,m, blue and red patches), while H^S_{12} and H^S_{23} both
535 remain dominant in their net effect. These patterns coincide with the region where energy fluxes are deflected.
536 Here, energy transfer is stronger for H^S_{12} than for H^S_{23} . Specifically, the background flow loses energy to the IT
537 modes: the Mode-2 background flow energizes the Mode-1 IT (Fig. 7n, red patches), and the Mode-3 background
538 flow energizes the Mode-2 IT (Fig. 7o, red patches). These overall patterns indicate a deflection of Mode-1 and
539 Mode-2 IT, and provide strong evidence for a dominant energy pathway from the background flow to the IT
540 modes driven by horizontal shear. This latter is coupled with direct forward energy transfer between IT modes
541 driven by topographic scattering previously observed.

542

543 In summary, in the CEC case, the interaction with the CE core dictates distinct fates for IT modes. Mode-1 IT
544 from sites A and D is not freely propagating but is primarily refracted into a single northward beam. In contrast,
545 Mode-2 IT is blocked, and Mode-3 IT is scattered at the eddy edge and seamount. Energy flux amplitudes for
546 Modes 1 and 2 exceed 200 W m^{-1} along their beams, whereas Mode-3 remains below this threshold. This
547 interaction facilitates a significant energy transfer ($O(\sim 10^{-8} \text{ W m kg}^{-1})$) governed by a complex interplay of two
548 mechanisms: 1) a dominant backward energy cascade, where horizontal shear transfers energy from the Mode-3
549 background flow to Mode-2 IT, and from the Mode-2 background flow to Mode-1 IT; and 2) a forward scattering,
550 where topography directly transfers energy from Mode-1 to Mode-3 IT.



551
 552 **Figure 7.** Tidal energy diagnostics for the CEC case (17 September 2015), following the format of Fig. 6.

553
 554 **3.2.3 CEE Case: IT Encountering a CE Edge**

555
 556 Finally, we assess IT interactions with the edge of a surface-intensified CE centered at 5.3° N, 45.0° W (radius
 557 143 km, maximum velocity 1.23 m s⁻¹, core bounded by 23–25.5 kg m⁻³ isopycnals extending ~100 m above the
 558 pycnocline).

559
 560 This interaction yields a different kinematic response. The incident Mode-1 energy fluxes from sites A and D
 561 converge and, at the eddy edge, clearly diffract into two distinct beams (Fig. 8a): one propagating northward

562 (~39°) and the other eastward (~35°) relative to their northeastward incident direction. The northward-refracted
563 beam maintains high HKE (150–200 J m⁻²), while HKE is sharply reduced (25–50 J m⁻²) in the northeast lee of
564 the CE (Fig. 8a). Separately, the eastward-refracted beam, less energetic (HKE <100 J m⁻²) than the northward
565 beam, passes near the eastern edge of a small AE. Mode-2 flux is sheared at the CE edge with limited directional
566 change (Fig. 8b), and Mode-3 becomes trapped along the northeastern CE edge and near the ridge (Fig. 8c).
567 Consistent with previous cases, Mode-1 and Mode-2 exhibit higher energy flux amplitudes (>200 W m⁻¹) than
568 Mode-3 (<200 W m⁻¹), and the energy flux patterns is supported by the vertical structures of the baroclinic velocity
569 (Appendix B, Figs. B1, B4).

570

571 As in prior cases, the analysis identified topographic scattering (C_{mn}) and horizontal shear (H_{mn}) of the background
572 flow as the two dominant mechanisms driving intermodal scattering in the CEE case.

573

574 The analysis of the term C_{mn} reveals a pattern modulated by the CE edge and seamount along the IT path from
575 sites A and D. A dominant forward energy transfer ($|C_{mn}| \sim 4 \times 10^{-8} \text{ W m kg}^{-1}$) from Mode-1 to Mode-2 for C_{12}
576 (Fig. 8e, blue patches) and from Mode-1 to Mode-3 IT for C_{13} (Fig. 8d, blue patches) occurs near the shelf break.
577 Near the eastern edge of the CE and the southern flank of the seamount, inter-modal IT energy transfers —
578 between Mode-1 and Mode-2 IT, and between Mode-2 and Mode-3 IT — are both strong and bidirectional (i.e.,
579 forward and backward transfers coexist; Figs. 8e,f, blue and red patches), and remain spatially confined to this
580 region. An exception is the Mode-1 to Mode-3 IT transfer (Fig. 8d), which is weak in this area.

581 These overall patterns indicate that the CE edge inhibits the forward energy cascade observed in the NE case and
582 instead initiates a dual mechanism: a potential flow shear-induced energy transfer between the background flow
583 (NECC/CE) and IT modes, and a topographically-driven energy scattering between IT modes.

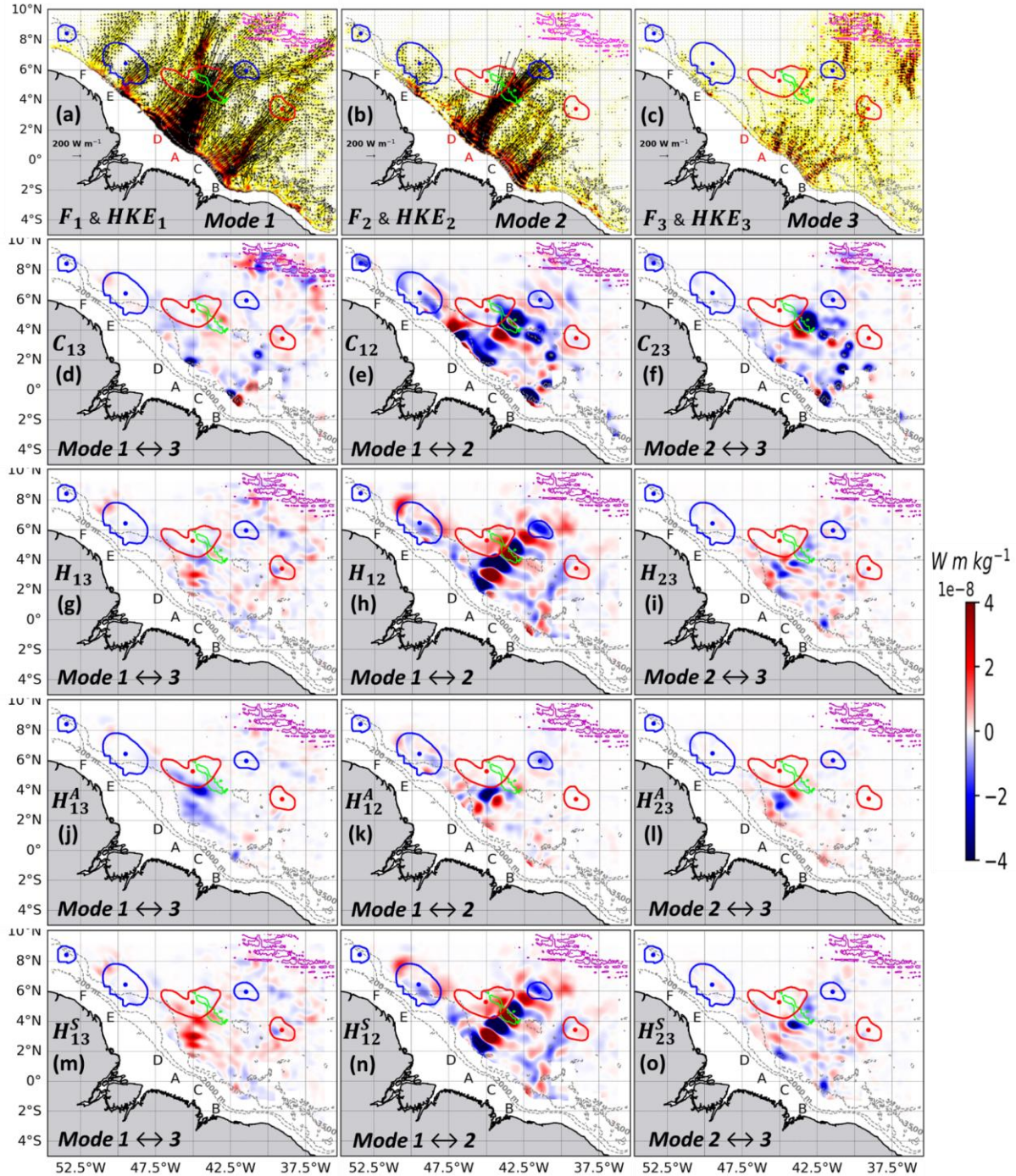
584

585 As in previous cases, the horizontal shear term (H_{mn}) in the CEE case is of comparable magnitude ($|H_{mn}| \sim 4 \times$
586 $10^{-8} \text{ W m}^{-1} \text{ kg}^{-1}$) to the topographic scattering term. The net effect of H_{mn} (Figs. 8g-i) is primarily dominated by
587 its symmetric part (Figs. 8m-o), except for term H_{13} . Along the IT path from sites A and D, terms H_{12}^S and H_{23}^S
588 are both strongly dominant in their net influence, while H_{13}^A and H_{13}^S weakly combine to form H_{13} (Figs. 8g,j,m)
589 — a pattern also present in the CEC case (Figs. 7g,j,m). The energy transfer pattern along this path is characterized
590 by alternating bands of energy loss and gain (blue and red patches), reflecting bidirectional transfers between the
591 background flow and IT modes. These alternating bands are particularly striking and spatially extended for H_{12}^S
592 (Figs. 8h,n). They are distinct from those observed in the previous cases, appearing both upstream and downstream
593 of the seamount and near the eastern CE edge. These patterns could result from an interference structure associated
594 with the IT field. For H_{23}^S , however, forward energy transfer dominates: the Mode-2 IT energizes the Mode-3
595 background flow near the CE edge (Fig. 8o, blue patches), coinciding with the region where energy fluxes are
596 deflected. These overall patterns provide strong evidence for a dominant energy pathway between the background
597 flow and IT modes driven by horizontal shear, coupled with a topographically-driven energy transfer between IT
598 modes.

599

600 In summary, in the CEE case, upon interacting with the CE edge, each IT mode meets a distinct fate. Mode-1 IT
601 from sites A and D splits into two energetic beams, propagating northward and eastward with energy fluxes

602 exceeding 200 W m^{-1} . In contrast, Mode-2 IT is sheared apart, while Mode-3 IT is scattered by the eddy edge and
 603 seafloor topography, its energy flux remaining below 200 W m^{-1} . During this encounter, a significant energy
 604 transfer ($\sim 10^{-8} \text{ W m kg}^{-1}$) occurs through dual mechanism distinct from that observed in the CEC case: 1) a
 605 dominant bidirectional energy transfer between the background flow and the IT modes (Mode-1 \leftrightarrow Mode-2 \leftrightarrow
 606 Mode-3) driven by horizontal shear, which can act to suppress the topographically-driven downscale energy, and
 607 2) a bidirectional energy transfer between the IT modes driven by topographic scattering.



608
 609

Figure 8. Tidal energy diagnostics for the CEE case (29 September 2015), following the format of Fig. 5.

610 **4 Discussion**

611 This study investigated the fate of M₂ IT energy on the Amazon shelf during the high EKE period of SOND 2015.
612 We addressed three questions: (1) Does the IT propagate freely, deviate, or become trapped by mesoscale features?
613 (2) Do these outcomes depend on the IT vertical mode, or on the location of the ME encounters (CE core vs. edge)
614 along with the associated background conditions (currents and stratification)? (3) What are the synergistic roles
615 of topography and CEs in governing modal energy transfers? By projecting energy flux into vertical modes and
616 performing intermodal energy transfer terms, we dissected these interactions more deeply.

617

618 **4.1 The Variable Fate of Internal Tides: Free Propagation, Deviation, and Trapping**

619

620 Our results show that the fate of IT energy is not uniform but is dictated by interactions with mesoscale features,
621 affecting the intensity and distribution of energy flux. The NE case established a baseline of efficient, long-range
622 propagation, where the Mode-1 energy flux maintained amplitudes exceeding 200 W m⁻¹ along a coherent beam
623 for over 1100 km. This free propagation aligns with previous studies (e.g., Xu et al., 2016; Fan et al., 2024) and
624 confirms Mode-1's characteristic as a freely propagating IT (Zhao et al., 2010). Its path is governed by Snell's
625 law (Small, 2001; Zhao, 2014), with minimal Coriolis constraint (f) near the equator ($f/\omega_{M2} \ll 1$, with ω_{M2} the M₂
626 tidal frequency), shifting steering mechanisms to wave–current and wave–stratification interactions. The stability
627 of the Mode-1 IT beam in background flow is consistent with ray-tracing results, such as those at the Hawaiian
628 Ridge, where typical currents had only slight effects (Rainville and Pinkel, 2006). While high-resolution and
629 idealized simulations suggested reduced Coriolis constraints at low latitudes (Wang et al., 2021; Le Dizes et al.,
630 2025), our realistic simulations advance these findings by forcing nonlinear interactions in a highly complex field.

631

632 In the NE case, the strong background flow—particularly the NECC—moved quasi-perpendicular to the incident
633 Mode-1 IT beams, and the associated stratification was notable over the seamount. The subcritical seamount
634 ($h_{\max}/H \sim 0.2$) acted only as a minor directional obstacle ($\lambda_1/w_{\max} \sim 0.9\text{--}1.25$) for propagating Mode-1 IT, though
635 it could affect higher-order modes intensified near the bottom.

636

637 In contrast, in the eddy cases, the incident Mode-1 IT beams passed through the strong cross-beam and along-
638 beam background flow (NECC/CE) in the CEC and CEE case, respectively. The presence of a CE consistently
639 disrupted free IT propagation, leading to deviation or trapping with distinct energy modulations. The incident
640 Mode-1 IT was deviated into convergent energy beams, creating a zone of reduced energy flux in the lee of the
641 eddy, consistent with processes modeled by Wang and Legg (2023) and Dunphy and Lamb (2014). This reduction
642 in coherent energy flux is strongly supported by in situ observations south of the Azores, which reported a
643 reduction in low-mode IT energy flux during interactions with a surface-intensified eddy (Löb et al., 2020). Across
644 all cases, Mode-3 energy never formed a coherent beam and consistently exhibited the weakest fluxes (<200 W
645 m⁻¹). The most relevant blockage occurred for Mode-2 (with flux amplitude comparable to Mode-1) in the CEC
646 case, where an otherwise energetic mode was completely impeded at the eddy–seamount interface. This
647 vulnerability aligns with global observations that Mode-2 M₂ IT generally has smaller sea surface height
648 amplitudes and shorter propagation distances (O[100 km]) than Mode-1 (Zhao, 2018). MEs thus act as potent
649 filters that selectively dissipate or trap the energy of specific vertical modes.

650 It should be noted that the multi-source interference, observed along the propagation paths of the energy fluxes
651 from sites A and D, could also modify the beam geometry independently of mesoscale activity. In this study, we
652 assume that the contribution of multi-source interference is smaller than that of eddy-induced effects. A more
653 detailed analysis would be required to precisely quantify this contribution.

654

655 **4.2 The Dual Control of IT Response: Vertical Mode and Eddy Encounters**

656

657 A key finding of this study is that the IT responses to an ME is dually controlled by its vertical mode, and the
658 specific location of the eddy encounter and its associated background conditions. Mode-1 IT is robust and long-
659 ranging but susceptible to beam steering, while Mode-2 is far more vulnerable to damping and blocking. Mode-3
660 IT is consistently weak and scattered, behaving as a trapped mode that seldom forms coherent beams. Only Mode-
661 1 IT underwent large-scale deviation by MEs or background flow fields, with energy loss occurring via forward
662 energy transfer at localized, energetic interaction sites (seamount, eddy boundaries). This is consistent with studies
663 showing that remote IT energy is scattered to higher modes at continental margins (Siyanbola et al., 2024; Fan et
664 al., 2024) and with findings that an ME focuses Mode-1 energy flux in specific areas while inducing vertical mode
665 scattering (Dunphy and Lamb, 2014). Our observation of Mode-1 deviation is analogous to the redirection of
666 ISWs by ME fields (Liao et al., 2012; Goret et al., 2026).

667

668 IT beam deviation is sensitive to eddy properties. The direction of deviation depends strongly on eddy polarity,
669 as shown by previous studies (e.g., Huang et al., 2018; Guo et al., 2023; Dunphy et al., 2017; Wang and Legg,
670 2023; Li et al., 2024; Goret et al., 2026). While the present study focuses exclusively on CEs, a qualitative
671 illustration of AE-induced deflection can be glimpsed in the energy flux path emanating from the less energetic
672 generation site E (Fig. 4b: deviation of the energy flux due to an AE core centered at 5.9°N and 48.5°W). While
673 earlier work noted that AE cores speed up Mode-1 propagation and induce clockwise (southward) refraction,
674 whereas CE cores slow it down and induce counterclockwise (northward) refraction, our findings link specific
675 interaction geometries to distinct intermodal energy pathways in a realistic framework. The impact of AEs on
676 intermodal energy pathways remains an important open question. Based on previous studies (e.g., Dunphy and
677 Lamb, 2014; Goret et al., 2026), we can assume that AEs exhibit a symmetric response; however, precise
678 quantification is left for future investigation.

679

680 The distinction between the CEC (core) and CEE (edge) cases reveals that the same CE can impose fundamentally
681 different fates on a passing Mode-1 IT beam. Interaction with the eddy core — where stratification was strong
682 and the CE flow was oriented cross-beam — refracted the incident beam coherently by $\sim 35^\circ$ into a single
683 northward path. In contrast, an encounter at the eddy edge — where stratification was quasi-uniform and the CE
684 flow was oriented along-beam — diffracted the energy into two distinct beams propagating northward ($\sim 39^\circ$) and
685 eastward ($\sim 35^\circ$). This demonstrates that “eddy lensing” is nuanced and sensitive to the radial structure and shear
686 fields of the eddy. Recent SWOT satellite observations corroborate this finding, documenting analogous refraction
687 near the eddy core and diffraction at a western eddy edge within the study region (Goret et al., 2026). Our results
688 provide a mechanistic explanation for incoherent IT signals and variable trapping noted in high-resolution models
689 of the ASOND period in this region (Tchilibou et al., 2022).

690

691 While Mode-1 IT is susceptible to beam steering, higher modes (Mode-2 and Mode-3) are more sensitive to
692 topography and are quickly damped, trapped, and become primary recipients of energy via downscale cascades
693 linked to topographic scattering (Lahaye et al., 2020; Fan et al., 2024; Bella et al., 2024). Our results advance
694 these findings by showing that higher modes are also more sensitive to the presence of a CE in conjunction with
695 a localized seamount. Therefore, the energy scattering from lower to higher IT modes and the trapping of those
696 modes by CE's flow are two linked processes facilitating the IT dissipation (Wang and Legg, 2023).

697

698 This study was limited to surface-intensified eddies. Future work should investigate whether similar IT
699 interactions occur with other ME types, such as deep intrathermocline eddies or complex multi-eddy systems. A
700 key question is whether eddies with thin vertical structures—and thus higher vertical modes—are capable of
701 trapping ITs, which warrants specific examination.

702

703 **4.3 Synergistic Roles of Topography, Background Flow, and CEs in Modal Energy Transfers**

704

705 Our results reveal a complex hierarchy of interactions that governs modal energy transfers, where even without
706 strong MEs, the combined effects of topography and background flow establish a baseline for energy pathways.

707

708 The NE case shows the seamount acts as a critical site for modal scattering, driving a dominant forward energy
709 cascade from Mode-1 to Mode-2 to Mode-3 IT ($\sim 4 \times 10^{-8} \text{ W m kg}^{-1}$). This magnitude of transfer is characteristic
710 of interactions over abrupt topography, consistent with quantifications of energy cascades on continental slopes
711 (Kelly and Nash, 2012). This topographically driven transfer is significantly modulated by background flow
712 (NECC, NBC) through horizontal shear mechanisms of comparable strength, aligning with studies in the North
713 Atlantic concluding that low-frequency flow strongly impacts the IT energy cycle, often transferring energy
714 toward smaller scales (Bella et al., 2024). Background flow shear actively participates in energy exchange,
715 facilitating transfer from the Mode-2 and Mode-3 background flow to the Mode-1 IT before the seamount, and
716 from the Mode-2 IT to the Mode-3 background flow over the seamount. Thus, seamount–topography interaction
717 with background flow creates a dynamic environment for energy redistribution even before considering ME
718 effects.

719

720 Introducing a CE—particularly one co-located with the seamount, as in the CEC case—fundamentally reorganizes
721 the energy transfer landscape. The CE's strong horizontal shear dominates background flow effects and reverses
722 the canonical energy pathway, initiating a dominant inverse energy cascade from background flow to IT modes.
723 This shift from the topographically driven forward cascade observed in the NE case is mediated by horizontal
724 shear, supported by analyses using coupled-mode shallow-water models that emphasize advection terms involving
725 mean flow and buoyancy shear (Kelly et al., 2016). The synergy between the CE and seamount creates competing
726 pathways: topographically driven forward scattering operates concurrently with eddy-driven inverse cascades,
727 leading to complex energy redistribution that explains observed modal blocking and trapping. This aligns with
728 studies detailing how CEs and AEs differently affect topographic scattering (Li et al., 2024) and underscores that
729 cross-scale energy exchange is a key driver in the tropical western Atlantic (Wang et al., 2025).

730

731 The consistent co-location of the CEs and the seamount with the NECC suggests the background conditions—
732 specifically western boundary currents—combined with the position of CE encounters, act to further enhance IT
733 refraction and diffraction. This mechanism is supported by studies in other western boundary currents (Duda et
734 al., 2018; Cao et al., 2022; Xu et al., 2021; Kelly and Lermusiaux, 2016; Chen et al., 2022; Pereira et al., 2007;
735 Kelly et al., 2016). However, fully isolating the individual contributions of the eddy flow from that of the NECC
736 will require a future idealized modelling framework.

737 **5 Conclusion**

738 This study illustrates the complex pathways of M2 IT energy in the region off the Amazon shelf during the period
739 of SOND 2015. By applying vertical mode decomposition to high-resolution NEMO-AMAZON36 simulations,
740 we examined three representative interaction cases: undisturbed propagation until crossing a topography,
741 interaction with a CE core, and interaction with a CE eastern edge. These three cases are schematically represented
742 in the figure 9. For each case, we systematically computed the intermodal energy transfer terms to identify the
743 governing mechanisms.

744

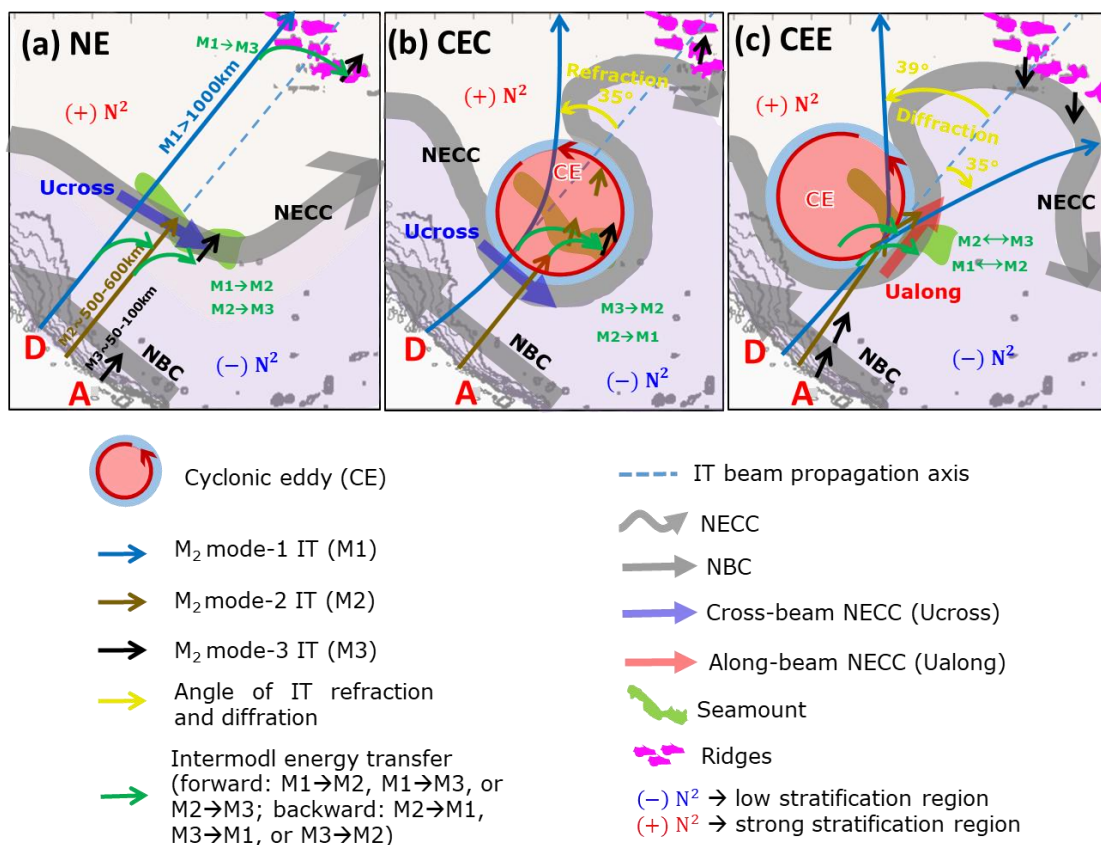
745 The two primary conclusions are as follows:

746 First, the specific response of an IT—whether it propagates freely or deviates—is dually controlled by IT vertical
747 modal structure, and the location of the ME encounters together with its associated background conditions
748 (currents and stratification). In the absence of a strong eddy (NE case, Fig. 9a), Mode-1 IT propagated freely as a
749 long-range coherent beam. It passed through the cross-beam NBC flow, crossed the Ceará Rise seamount, and
750 continued through the cross-beam NECC flow — the latter associated with strong stratification — with little
751 disruption. In contrast, interactions with a CE and its associated currents and stratification consistently disrupted
752 this propagation pattern, leading to refraction, diffraction, or trapping. When the beam encountered the CE core
753 (CEC case, Fig. 9b), where stratification was strong and the CE flow was oriented cross-beam, the Mode-1 beam
754 was coherently refracted northward by approximately 35° while maintaining high energy fluxes ($>200 \text{ W m}^{-1}$).
755 At the eddy edge (CEE case, Fig. 9c), however, where stratification was quasi-uniform and the CE flow was
756 oriented along-beam, the beam instead underwent diffraction: its energy split into two distinct beams propagating
757 northward ($\sim 39^\circ$) and eastward ($\sim 35^\circ$). Higher modes were particularly susceptible to trapping; Mode-2 energy
758 flux—despite an amplitude comparable to Mode-1—was completely blocked and trapped at the eddy-seamount
759 interface, while Mode-3 energy remained weak ($<200 \text{ W m}^{-1}$), scattered and less blocked. This weaker and more
760 spatially diffuse signature of mode 3, in contrast to the clearly blocked mode 2, likely reflects local generation
761 near the seamount and/or a loss of coherence induced by the overlying eddy, and deserves future investigation.

762

763 Second, the redistribution of energy via intermodal transfers is governed by a hierarchy of synergistic interactions
764 between the seamount and the background flow of the eddy. In the NE case, the seamount drives a dominant
765 forward energy cascade from Mode-1 to higher modes ($O(10^{-8} \text{ W m kg}^{-1})$), a process modulated by the
766 background flow's horizontal shear. The presence of a CE colocated with the seamount fundamentally reorganizes
767 this dynamic. The CE's strong horizontal shear initiates a dominant inverse energy cascade from the background

768 flow to the IT modes, directly competing with the ongoing topographic forward cascade. This specific synergy is
 769 crucial for explaining the extreme blocking of Mode-2 and the complex redistribution of energy fluxes observed.
 770
 771 Nonetheless, the region is shaped by a complex, co-located interplay of forces—including the NECC, MEs (CEs
 772 and AEs), and the topographic features—making it challenging to fully isolate their individual effects on ITs in
 773 our realistic simulations. Limiting our analysis to three case studies reflects the primarily qualitative nature of our
 774 approach. A natural next step would be to extend it toward more quantitative results by conducting composite
 775 analyses over a larger set of eddy-IT interaction cases. Grouping configurations by eddy position relative to the
 776 seamount, for instance, would allow the IT responses to mesoscale variability to be characterized in a statistically
 777 robust way. In addition to statistical analyses, to disentangle and quantify the specific contributions of each
 778 mesoscale feature with greater precision, future work should also employ idealized modelling frameworks. Such
 779 an approach is essential for isolating the deterministic impacts of mesoscale flow and advancing toward a
 780 predictive understanding of IT energy pathways in complex oceanic environments.
 781 Finally, it should be noted that the use of flat-bottom vertical modes in the vicinity of steep topography represents
 782 a limitation of our analysis, particularly for diagnosing higher-mode energy transfers near the seamount. Future
 783 work employing topography-aware modal decompositions would help refine these results and provide a more
 784 accurate representation of IT energetics.



785
 786 **Figure 9.** Schematics summarizing the fate of propagating M2 IT from generation sites A and D on the Amazon
 787 shelf-break. The panels correspond to the three analyzed cases: (a) NE, (b) CEC, and (c) CEE. The diagram
 788 highlights the key dynamic IT responses—inter-modal scattering, refraction, and diffraction—resulting from
 789 interaction with mesoscale structures, emphasizing the pronounced effects of CEs. The specific IT response is

790 dually controlled by its vertical mode, and the CE encounter location along with the associated background
791 conditions. Furthermore, intermodal energy scattering is governed by a hierarchical synergy between the seamount
792 and the CE's background flow.

793

794 **Data availability**

795 The AMAZON36 simulations are available upon request by contacting the corresponding author.

796

797 **Authors contributions**

798 Funding acquisition: AKL, XC and MA. Conceptualization and methodology: FK, AKL and XC. Performing
799 simulations: FA and GM with the assistance of AKL. Data processing: FK. Formal analysis: FK with interactions
800 from all co-authors. Preparation and writing of the manuscript: FK with contributions from all co-authors.

801

802 **Competing interests**

803 The contact author has declared that none of the authors has any competing interests.

804

805 **Acknowledgments**

806 This work is a contribution to the TOSCA project MIAMAZ-ETI (Multi-Sensors study of the fine scale processes
807 and their impacts on ocean color, off the Amazon shelf: Eddy-Tides Interactions).

808

809 **Financial support**

810 This work is part of the PhD thesis of Fabius Kouogang, conducted under the joint supervision of Ariane Koch-
811 Larrouy, Xavier Carton, and Moacyr Araujo. The research received support from "Coordenação de
812 Aperfeiçoamento de Pessoal de Nível Superior" (CAPES); the Institute of Research for Development (IRD,
813 France) via an ARTS grant; the ISblue project, Interdisciplinary graduate school for the blue planet (ANR-17-
814 EURE-0015) and co-funded by a grant from the French government under the program "Investissements d'Avenir"
815 embedded in France 2030; and the "Centre National d'Études Spatiales" (CNES) through the TOSCA project
816 MIAMAZ-ETI (Principal Investigators: Ariane Koch-Larrouy, Camila Artana, Isabelle Dadou). Moacyr Araujo
817 was funded by the Brazilian National Council for Scientific and Technological Development (CNPq), and Xavier
818 Carton received support from the University of Western Brittany.

819

820 **References**

821 Aguedjou, H. M. A., Dadou, I., Chaigneau, A., Morel, Y., and Alory, G.: Eddies in the tropical Atlantic Ocean
822 and their seasonal variability, *Geophys. Res. Lett.*, 46, 12156–12164, <https://doi.org/10.1029/2019GL083925>,
823 2019.

824

825 Aguedjou, H. M. A., Chaigneau, A., Dadou, I., Morel, Y., Pegliasco, C., Da-Allada, C. Y., and Baloitcha, E.:
826 What can we learn from observed temperature and salinity isopycnal anomalies at eddy generation sites?
827 Application in the tropical Atlantic Ocean, *J. Geophys. Res.: Oceans*, 126, e2021JC017630,
828 <https://doi.org/10.1029/2021JC017630>, 2021.

829

830 Alford, M. H., Simmons, H. L., Marques, O. B., and Girton, J. B.: Internal tide attenuation in the North Pacific,
831 *Geophys. Res. Lett.*, 46, 8205–8213, <https://doi.org/10.1029/2019GL082648>, 2019.

832

833 Alford, M. H., and Zhao, Z.: Global patterns of low-mode internal-wave propagation. Part I: Energy and energy
834 flux, *J. Phys. Oceanogr.*, 37, 1829–1848, <https://doi.org/10.1175/jpo3085.1>, 2007.

835

836 Assene, F., Koch-Larrouy, A., Dadou, I., Tchilibou, M., Morvan, G., Chanut, J., Costa Da Silva, A., Vantrepotte,
837 V., Allain, D., and Tran, T.-K.: Internal tides off the Amazon shelf – Part 1: The importance of the structuring of
838 ocean temperature during two contrasted seasons, *Ocean Sci.*, 20, 43–67, <https://doi.org/10.5194/os-20-43-2024>,
839 2024.

840

841 Barbot, S., Lyard, F., Tchilibou, M., and Carrere, L.: Background stratification impacts on internal tide generation
842 and abyssal propagation in the western equatorial Atlantic and the Bay of Biscay, *Ocean Sci.*, 17, 1563–1583,
843 <https://doi.org/10.5194/os-17-1563-2021>, 2021.

844

845 Barnier, B., Reynaud, T., Beckmann, A., Böning, C., Molines, J.-M., Barnard, S., and Jia, Y.: On the seasonal
846 variability and eddies in the North Brazil Current: Insights from model intercomparison experiments, *Prog.*
847 *Oceanogr.*, 48, 195–230, [https://doi.org/10.1016/S0079-6611\(01\)00005-2](https://doi.org/10.1016/S0079-6611(01)00005-2), 2001.

848

849 Bella, A., Lahaye, N., and Tissot, G.: Internal tide energy transfers induced by mesoscale circulation and
850 topography across the North Atlantic, *J. Geophys. Res.: Oceans*, 129, e2024JC020914,
851 <https://doi.org/10.1029/2024JC020914>, 2024.

852

853 Brandt, P., Rubino, A., and Fischer, J.: Large-amplitude internal solitary waves in the North Equatorial
854 Countercurrent, *J. Phys. Oceanogr.*, 32, 1567–1573, [https://doi.org/10.1175/1520-0485\(2002\)032<1567:LAI SWI>2.0.CO;2](https://doi.org/10.1175/1520-0485(2002)032<1567:LAI SWI>2.0.CO;2), 2002.

855

856

857 Buijsman, M. C., Legg, S., and Klymak, J.: Double-ridge internal tide interference and its effect on dissipation in
858 Luzon Strait, *J. Phys. Oceanogr.*, 42, 1337–1356, <https://doi.org/10.1175/jpo-d-11-0210.1>, 2012.

859

860 Cao, A., Guo, Z., Wang, S., Guo, X., and Song, J.: Incoherence of the M2 and K1 internal tides radiated from the
861 Luzon Strait under the influence of looping and leaping Kuroshio, *Prog. Oceanogr.*, 206, 102850,
862 <https://doi.org/10.1016/j.pocean.2022.102850>, 2022.

863

864 Chen, J., Zhu, X.-H., Wang, M., Zheng, H., Zhao, R., Nakamura, H., and Yamashiro, T.: Incoherent signatures of
865 internal tides in the Tokara Strait modulated by the Kuroshio, *Prog. Oceanogr.*, 206, 102863,
866 <https://doi.org/10.1016/j.pocean.2022.102863>, 2022.

867

868 Clément, L., Frajka-Williams, E., Sheen, K. L., Brearley, J. A., and Garabato, A. N.: Generation of internal waves
869 by eddies impinging on the western boundary of the North Atlantic, *J. Phys. Oceanogr.*, 46, 1067–1079,
870 <https://doi.org/10.1175/JPO-D-14-0241.1>, 2016.

871

872 De Macedo, C. R., Koch-Larrouy, A., Da Silva, J. C. B., Magalhães, J. M., Lentini, C. A. D., Tran, T. K., Rosa,
873 M. C. B., and Vantrepotte, V.: Spatial and temporal variability of mode-1 and mode-2 internal solitary waves from
874 MODIS/TERRA sunglint off the Amazon shelf, *Ocean Sci.*, 19, 1357–1374, [https://doi.org/10.5194/os-19-1357-](https://doi.org/10.5194/os-19-1357-2023)
875 2023, 2023.

876

877 Delpech, A., Cravatte, S., Marin, F., Morel, Y., Gronchi, E., and Kestenare, E.: Observed tracer fields structuration
878 by middepth zonal jets in the tropical Pacific, *J. Phys. Oceanogr.*, 50, 281–304, [https://doi.org/10.1175/JPO-D-](https://doi.org/10.1175/JPO-D-19-0091.1)
879 19-0091.1, 2020.

880

881 Didden, N., and Schott, F.: Eddies in the North Brazil Current retroflexion region observed by Geosat altimetry,
882 *J. Geophys. Res.*, 98, 20121, <https://doi.org/10.1029/93JC01184>, 1993.

883

884 Duda, T. F., Lin, Y.-T., Buijsman, M., and Newhall, A. E.: Internal tidal modal ray refraction and energy ducting
885 in baroclinic Gulf Stream currents, *J. Phys. Oceanogr.*, 48, 1965–1983, <https://doi.org/10.1175/JPO-D-17-0230.1>,
886 2018.

887

888 Dunphy, M., and Lamb, K. G.: Focusing and vertical mode scattering of the first mode internal tide by mesoscale
889 eddy interaction, *J. Geophys. Res.: Oceans*, 119, 523–536, <https://doi.org/10.1002/2013JC009363>, 2014.

890

891 Dunphy, M., Ponte, A. L., Klein, P., and Le Gentil, S.: Low-mode internal tide propagation in a turbulent eddy
892 field, *J. Phys. Oceanogr.*, 47, 649–665, <https://doi.org/10.1175/JPO-D-16-0099.1>, 2017.

893

894 Ernst, P. A., Subrahmanyam, B., Morel, Y., Trott, C. B., and Chaigneau, A.: Subsurface eddy detection optimized
895 with potential vorticity from models in the Arabian Sea, *J. Atmos. Ocean. Technol.*, 40, 677–700,
896 <https://doi.org/10.1175/JTECH-D-22-0050.1>, 2023.

897

898 Ertel, H.: On hydrodynamic eddy theorems, *Phys. Z.*, 43, 526–529, 1942.

899

900 Fan, L., Sun, H., Yang, Q., and Li, J.: Numerical investigation of interaction between anticyclonic eddy and
901 semidiurnal internal tide in the northeastern South China Sea, *Ocean Sci.*, 20, 241–264, [https://doi.org/10.5194/os-](https://doi.org/10.5194/os-20-241-2024)
902 20-241-2024, 2024.

903

904 Fassoni-Andrade, A. C., Durand, F., Azevedo, A., Bertin, X., Santos, L. G., Khan, J. U., Testut, L., and Moreira,
905 D. M.: Seasonal to interannual variability of the tide in the Amazon estuary, *Cont. Shelf Res.*, 255, 104945,
906 <https://doi.org/10.1016/j.csr.2023.104945>, 2023.

907

908 Fratantoni, D. M., and Glickson, D. A.: North Brazil Current Ring generation and evolution observed with
909 SeaWiFS, *J. Phys. Oceanogr.*, 32, 1058–1074, [https://doi.org/10.1175/1520-0485\(2002\)032<1058:NBCRGA>2.0.CO;2](https://doi.org/10.1175/1520-0485(2002)032<1058:NBCRGA>2.0.CO;2), 2002.

911

912 Gabioux, M., Vinzon, S.B., Paiva, A.M.: Tidal propagation over fluid mud layers on the Amazon shelf,
913 *Continental Shelf Research*, 25, 113–125, <https://doi.org/10.1016/j.csr.2004.09.001>, 2005.

914

915 Garrett, C., and Kunze, E.: Internal tide generation in the deep ocean, *Annu. Rev. Fluid Mech.*, 39, 57–87,
916 <https://doi.org/10.1146/ANNUREV.FLUID.39.050905.110227>, 2007.

917

918 Gerkema, T., and Zimmerman, J. T. F.: An introduction to internal waves, Lecture Notes, Royal Netherlands
919 Institute for Sea Research, 2008.

920

921 Goret, C., Koch-Larrouy, A., Kouogang, F., de Macedo, C. R., M’Hamdi, A., Magalhães, J., da Silva, J. C. B.,
922 Tchilibou, M., Artana, C., Dadou, I., Delepouille, A., Barbot, S., Ballarotta, M., Carrère, L., and Costa da Silva,
923 A.: Internal solitary waves refraction and diffraction from interaction with eddies off the Amazon shelf from
924 SWOT, EGU sphere [preprint], <https://doi.org/10.5194/egusphere-2025-3933>, 2026.

925

926 Guo, Z., Wang, S., Cao, A., Xie, J., Song, J., and Guo, X.: Refraction of the M2 internal tides by mesoscale eddies
927 in the South China Sea, *Deep-Sea Res. Pt. I*, 192, 103946, <https://doi.org/10.1016/j.dsr.2022.103946>, 2023.

928

929 Huang, X., Wang, Z., Zhang, Z., Yang, Y., Zhou, C., Yang, Q., Zhao, W., and Tian, J.: Role of mesoscale eddies
930 in modulating the semidiurnal internal tide: Observation results in the northern South China Sea, *J. Phys.*
931 *Oceanogr.*, 48, 1749–1768, <https://doi.org/10.1175/JPO-D-17-0238.1>, 2018.

932

933 Johnston, T. M. S., and Merrifield, M. A.: Internal tide scattering at the Line Islands Ridge, *J. Geophys. Res.*, 108,
934 3365, <https://doi.org/10.1029/2003JC001844>, 2003.

935

936 Kelly, S. M.: The vertical mode decomposition of surface and internal tides in the presence of a free surface and
937 arbitrary topography, *J. Phys. Oceanogr.*, 46, 3845–3859, <https://doi.org/10.1175/JPO-D-16-0164.1>, 2016.

938

939 Kelly, S. M., and Lermusiaux, P. F. J.: The cascade of tidal energy from low to high modes on a continental slope,
940 *J. Phys. Oceanogr.*, 42, 1276–1292, <https://doi.org/10.1175/JPO-D-11-0231.1>, 2012.

941

942 Kelly, S. M., and Lermusiaux, P. F. J.: Internal-tide interactions with the Gulf Stream and Middle Atlantic Bight
943 shelfbreak front, *J. Geophys. Res.: Oceans*, 121, 6271–6294, <https://doi.org/10.1002/2016JC011986>, 2016.

944

945 Kelly, S. M., Lermusiaux, P. F. J., and Duda, T. F.: A coupled-mode shallow-water model for tidal analysis:
946 Internal tide reflection and refraction by the Gulf Stream, *J. Phys. Oceanogr.*, 46, 3747–3767,
947 <https://doi.org/10.1175/JPO-D-16-0125.1>, 2016.

948
949 Kelly, S. M., Nash, J. D., Martini, K. I., Alford, M. H., and Kunze, E.: The cascade of tidal energy from low to
950 high modes on a continental slope, *J. Phys. Oceanogr.*, 42, 1217–1232, <https://doi.org/10.1175/jpo-d-11-0231.1>,
951 2012.
952
953 Kelly, S. M., Nash, J. D., and Kunze, E.: Internal-tide energy over topography, *J. Geophys. Res.-Oceans*, 115,
954 C06014, <https://doi.org/10.1029/2009JC005618>, 2010.
955
956 Kelly, S. M., and Nash, J. D.: Internal-tide generation and destruction by shoaling internal tides, *Geophys. Res.*
957 *Lett.*, 37, L23611, <https://doi.org/10.1029/2010GL045598>, 2010.
958
959 Kerry, C. G., Powell, B. S., and Carter, G. S.: Effects of remote generation sites on model estimates of M2 internal
960 tides in the Philippine Sea, *J. Phys. Oceanogr.*, 43, 187–204, <https://doi.org/10.1175/jpo-d-12-081.1>, 2013.
961
962 Koch-Larrouy, A., Atmadipoera, A., van Beek, P., Madec, G., Aucan, J., Lyard, F., Grelet, J., and Souhaut, M.:
963 Estimates of tidal mixing in the Indonesian archipelago from multidisciplinary INDOMIX in-situ data, *Deep-Sea*
964 *Res. Pt. I*, 106, 136–153, <https://doi.org/10.1016/j.dsr.2015.09.007>, 2015.
965
966 Kouogang, F., Koch-Larrouy, A., Magalhaes, J., Costa Da Silva, A., Kerhervé, D., Bertrand, A., Cervelli, E.,
967 TERNON, J.-F., Roussetot, P., Lee, J., Rollnic, M., and Araujo, M.: Turbulent dissipation from AMAZOMIX off
968 the Amazon shelf along internal tide paths, *Ocean Sci.*, 21, 1589–1608, <https://doi.org/10.5194/os-21-1589-2025>,
969 2025.
970
971 Kunze, E.: Internal-wave-driven mixing: Global geography and budgets, *J. Phys. Oceanogr.*, 47, 1325–1345,
972 <https://doi.org/10.1175/JPO-D-16-0141.1>, 2017.
973
974 Kurian, J., Colas, F., Capet, X., McWilliams, J. C., and Chelton, D. B.: Eddy properties in the California Current
975 System, *J. Geophys. Res.-Oceans*, 116, <https://doi.org/10.1029/2010jc006895>, 2011.
976
977 Lahaye, N., Gula, J., and Roullet, G.: Internal tide cycle and topographic scattering over the north mid-Atlantic
978 ridge, *J. Geophys. Res.: Oceans*, 125, e2020JC016376, <https://doi.org/10.1029/2020JC016376>, 2020.
979
980 Lahaye, N., Ponte, A., Le Sommer, J., and Albert, A.: Internal tide surface signature and incoherence in the North
981 Atlantic, *Geophys. Res. Lett.*, 51, e2024GL108508, <https://doi.org/10.1029/2024GL108508>, 2024.
982
983 Le Dizes, C., Grisouard, N., Thual, O., and Mercier, M. J.: Three-dimensional modelling of internal tide
984 generation over isolated seamounts in a rotating ocean, *J. Fluid Mech.*, 1022, A5,
985 <https://doi.org/10.1017/jfm.2025.10647>, 2025.
986

987 Li, B., Xu, M., Chen, W., Yuan, Y., Liu, Y., and Li, S.: Evolution of internal tide scattering hidden below
 988 mesoscale eddies, *Prog. Oceanogr.*, 226, 103305, <https://doi.org/10.1016/j.pocean.2024.103305>, 2024.
 989
 990 Liao, G., Yang, C., Xu, X., Shi, X., Yuan, Y., and Huang, W.: Effects of mesoscale eddies on the internal solitary
 991 wave propagation, *Acta Oceanol. Sin.*, 31, 26–40, <https://doi.org/10.1007/s13131-012-0205-5>, 2012.
 992
 993 Lorenz, E. N.: Available potential energy and the maintenance of the general circulation, *Tellus*, 7, 157–167,
 994 <https://doi.org/10.1111/j.2153-3490.1955.tb01148.x>, 1955.
 995
 996 Löb, J., Köhler, J., Mertens, C., Walter, M., Li, Z., and von Storch, J.-S.: Observations of the low-mode internal
 997 tide and its interaction with mesoscale flow south of the Azores, *J. Geophys. Res.: Oceans*, 125, e2019JC015879,
 998 <https://doi.org/10.1029/2019JC015879>, 2020.
 999
 1000 Madec, G., Bourdallé-Badie, R., Chanut, J., Clementi, E., Coward, A., Ethé, C., Iovino, D., Lea, D., Lévy, C.,
 1001 Lovato, T., Martin, N., Masson, S., Mocavero, S., Rousset, C., Storkey, D., Vancoppenolle, M., Müeller, S.,
 1002 Nurser, G., Bell, M., and Samson, G.: NEMO ocean engine, Zenodo, <https://doi.org/10.5281/zenodo.3878122>,
 1003 2019.
 1004
 1005 Magalhaes, J. M., Da Silva, J. C. B., Buijsman, M. C., and Garcia, C. A. E.: Effect of the North Equatorial Counter
 1006 Current on the generation and propagation of internal solitary waves off the Amazon shelf (SAR observations),
 1007 *Ocean Sci.*, 12, 243–255, <https://doi.org/10.5194/os-12-243-2016>, 2016.
 1008
 1009 Mathur, M., Carter, G. S., and Peacock, T.: Topographic scattering of the low-mode internal tide in the deep
 1010 ocean, *J. Geophys. Res.-Oceans*, 119, 2165–2182, <https://doi.org/10.1002/2013JC009152>, 2014.
 1011
 1012 Morel, Y., Gula, J., and Ponte, A.: Potential vorticity diagnostics based on balances between volume integral and
 1013 boundary conditions, *Ocean Model.*, 138, 23–35, <https://doi.org/10.1016/j.ocemod.2019.04.004>, 2019.
 1014
 1015 Morel, Y., Morvan, G., Benshila, R., Renault, L., Gula, J., and Auclair, F.: An “objective” definition of potential
 1016 vorticity: Generalized evolution equation and application to the study of coastal upwelling instability, *Ocean*
 1017 *Model.*, 186, 102287, <https://doi.org/10.1016/j.ocemod.2023.102287>, 2023.
 1018
 1019 Nakamura, N.: Modified Lagrangian-mean diagnostics of the stratospheric polar vortices. Part I. Formulation and
 1020 analysis of GFDL SKYHI GCM, *J. Atmos. Sci.*, 52, 2096–2108, [https://doi.org/10.1175/1520-0469\(1995\)052<2096:MLMDOT>2.0.CO;2](https://doi.org/10.1175/1520-0469(1995)052<2096:MLMDOT>2.0.CO;2), 1995.
 1021
 1022
 1023 Nash, J. D., Kelly, S. M., Shroyer, E. L., Moum, J. N., and Duda, T. F.: The unpredictable nature of internal tides
 1024 on continental shelves, *J. Phys. Oceanogr.*, 42, 1981–2000, <https://doi.org/10.1175/JPO-D-12-028.1>, 2012.
 1025

1026 Okubo, A.: Horizontal dispersion of floatable particles in vicinity of velocity singularities such as convergence,
1027 Deep-Sea Res., 17, 445, [https://doi.org/10.1016/0011-7471\(70\)90059-8](https://doi.org/10.1016/0011-7471(70)90059-8), 1970.
1028

1029 Pereira, A. F., Castro, B. M., Calado, L., and da Silveira, I. C. A.: Numerical simulation of M2 internal tides in
1030 the South Brazil Bight and their interaction with the Brazil Current, J. Geophys. Res., 112, C04009,
1031 <https://doi.org/10.1029/2006JC003673>, 2007.
1032

1033 Rainville, L., and Pinkel, R.: Propagation of low-mode internal waves through the ocean, J. Phys. Oceanogr., 36,
1034 1220–1236, <https://doi.org/10.1175/JPO2924.1>, 2006.
1035

1036 Savage, A. C., Waterhouse, A. F., and Kelly, S. M.: Internal tide nonstationarity and wave–mesoscale interactions
1037 in the Tasman Sea, J. Phys. Oceanogr., 50, 2931–2951, <https://doi.org/10.1175/JPO-D-20-0081.1>, 2020.
1038

1039 Silva, A. C., Bourles, B., and Araujo, M.: Circulation of the thermocline salinity maximum waters off the Northern
1040 Brazil as inferred from in situ measurements and numerical results, Ann. Geophys., 27, 1861–1873,
1041 <https://doi.org/10.5194/angeo-27-1861-2009>, 2009.
1042

1043 Siyanbola, O. Q., Buijsman, M. C., Delpéch, A., Barkan, R., Pan, Y., and Arbic, B. K.: Interactions of remotely
1044 generated internal tides with the U.S. West Coast continental margin, J. Geophys. Res.: Oceans, 129,
1045 e2023JC020859, <https://doi.org/10.1029/2023JC020859>, 2024.
1046

1047 Small, J.: A nonlinear model of the shoaling and refraction of interfacial solitary waves in the ocean. Part II:
1048 Oblique refraction across a continental slope and propagation over a seamount, J. Phys. Oceanogr., 31, 3184–
1049 3199, [https://doi.org/10.1175/1520-0485\(2001\)031<3184:ANMOTS>2.0.CO;2](https://doi.org/10.1175/1520-0485(2001)031<3184:ANMOTS>2.0.CO;2), 2001.
1050

1051 Tchilibou, M., Gourdeau, L., Lyard, F., Morrow, R., Koch Larrouy, A., Allain, D., and Djath, B.: Internal tides in
1052 the Solomon Sea in contrasted ENSO conditions, Ocean Sci., 16, 615–635, [https://doi.org/10.5194/os-16-615-](https://doi.org/10.5194/os-16-615-2020)
1053 2020, 2020.
1054

1055 Tchilibou, M., Koch-Larrouy, A., Barbot, S., Lyard, F., Morel, Y., Jouanno, J., and Morrow, R.: Internal tides off
1056 the Amazon shelf during two contrasted seasons: Interactions with background circulation and SSH imprints,
1057 Ocean Sci., 18, 1591–1618, <https://doi.org/10.5194/os-18-1591-2022>, 2022.
1058

1059 Vic, C., Naveira Garabato, A. C., Green, J. M., Waterhouse, A. F., Zhao, Z., Melet, A., de Lavergne, C., Buijsman,
1060 M. C., and Stephenson, G. R.: Deep-ocean mixing driven by small-scale internal tides, Nat. Commun., 10, 2099,
1061 <https://doi.org/10.1038/s41467-019-10149-5>, 2019.
1062

1063 Wang, W., Li, J., and Huang, X.: Semidiurnal internal tide interference in the northern South China Sea, J. Marine
1064 Sci. Eng., 12, 811, <https://doi.org/10.3390/jmse12050811>, 2024.
1065

1066 Wang, X., Peng, S., Liu, Z., Huang, R. X., Qian, Y.-K., and Li, Y.: Tidal mixing in the South China Sea: An
1067 estimate based on the internal tide energetics, *J. Phys. Oceanogr.*, 46, 107–124, [https://doi.org/10.1175/JPO-D-](https://doi.org/10.1175/JPO-D-15-0082.1)
1068 15-0082.1, 2016.

1069

1070 Wang, Y., Curchitser, E., Legg, S., and Kang, D.: Internal tide interactions with submesoscale and mesoscale
1071 eddies in the tropical western Atlantic, *J. Phys. Oceanogr.*, 55, 1245–1262, [https://doi.org/10.1175/JPO-D-24-](https://doi.org/10.1175/JPO-D-24-0063.1)
1072 0063.1, 2025.

1073

1074 Wang, Y., and Legg, S.: Enhanced dissipation of internal tides in a mesoscale baroclinic eddy, *J. Phys. Oceanogr.*,
1075 53, 2533–2550, <https://doi.org/10.1175/JPO-D-22-0205.1>, 2023.

1076

1077 Wang, Y., Xu, Z., Hibiya, T., Yin, B., and Wang, F.: Radiation path of diurnal internal tides in the northwestern
1078 Pacific controlled by refraction and interference, *J. Geophys. Res.: Oceans*, 126, e2020JC016972,
1079 <https://doi.org/10.1029/2020JC016972>, 2021.

1080

1081 Waterhouse, A. F., Kelly, S. M., Zhao, Z., MacKinnon, J. A., Nash, J. D., Simmons, H., and Pinkel, R.:
1082 Observations of the Tasman Sea internal tide beam, *J. Phys. Oceanogr.*, 48, 1283–1297,
1083 <https://doi.org/10.1175/JPO-D-17-0116>, 2018.

1084

1085 Weiss, J.: The dynamics of enstrophy transfer in 2-dimensional hydrodynamics, *Physica D*, 48, 273–294,
1086 [https://doi.org/10.1016/0167-2789\(91\)90088-Q](https://doi.org/10.1016/0167-2789(91)90088-Q), 1991.

1087

1088 Winters, K. B., and D’Asaro, E. A.: Diascalar flux and the rate of fluid mixing, *J. Fluid Mech.*, 317, 179–193,
1089 <https://doi.org/10.1017/S002211209600007X>, 1996.

1090

1091 Wunsch, C., and Ferrari, R.: Vertical mixing, energy, and the general circulation of the oceans, *Annu. Rev. Fluid*
1092 *Mech.*, 36, 281–314, <https://doi.org/10.1146/annurev.fluid.36.050802.122121>, 2004.

1093

1094 Xu, A., Yu, F., and Nan, F.: Study of subsurface eddy properties in northwestern Pacific Ocean based on an eddy-
1095 resolving OGCM, *Ocean Dynam.*, 69, 463–474, <https://doi.org/10.1007/s10236-019-01255-5>, 2019.

1096

1097 Xu, Z., Liu, K., Yin, B., Zhao, Z., Wang, Y., and Li, Q.: Longrange propagation and associated variability of
1098 internal tides in the South China Sea, *J. Geophys. Res.-Oceans*, 121, 8268–8286,
1099 <https://doi.org/10.1002/2016JC012105>, 2016.

1100

1101 Xu, Z., Wang, Y., Liu, Z., McWilliams, J. C., and Gan, J.: Insight into the dynamics of the radiating internal tide
1102 associated with the Kuroshio current, *J. Geophys. Res.: Oceans*, 126, e2020JC017018,
1103 <https://doi.org/10.1029/2020JC017018>, 2021.

1104

1105 Zhao, Z.: The global mode-2 M2 internal tide, *J. Geophys. Res.: Oceans*, 123, 7725–7746,
1106 <https://doi.org/10.1029/2018JC014380>, 2018.

1107

1108 Zhao, Z.: Internal tide radiation from the Luzon Strait, *J. Geophys. Res.: Oceans*, 119, 5434–5448,
1109 <https://doi.org/10.1002/2014JC010150>, 2014.

1110

1111 Zhao, Z., Alford, M. H., MacKinnon, J. A., and Pinkel, R.: Long-range propagation of the semidiurnal internal
1112 tide from the Hawaiian Ridge, *J. Phys. Oceanogr.*, 40, 713–736, <https://doi.org/10.1175/2009JPO4207.1>, 2010.

1113

1114 Zhao, Z.: The global mode-1 S2 internal tide, *J. Geophys. Res.-Oceans*, 122, 8794–8812,
1115 <https://doi.org/10.1002/2017JC013112>, 2017.

1116

1117 Zaron, E. D., and Egbert, G. D.: Time-variable refraction of internal tides at the Hawaiian Ridge, *J. Phys.*
1118 *Oceanogr.*, 44, 538–557, <https://doi.org/10.1175/JPO-D-12-0238.1>, 2014.

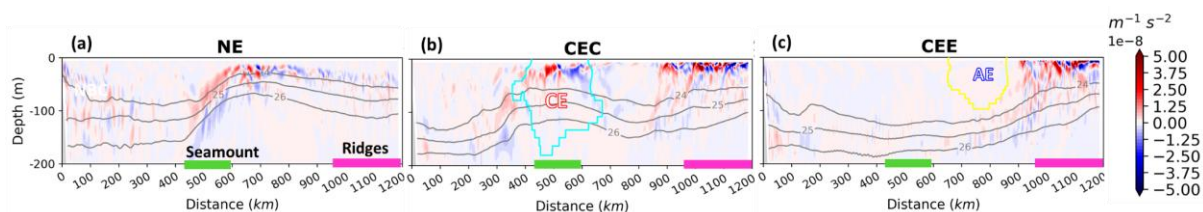
1119

1120 Appendix

1121

1122 Appendix A: Horizontal Stratification Gradients Along IT Paths

1123 To evaluate the background stratification in the NE, CEC, and CEE cases, we computed the horizontal
1124 stratification gradient (∇N^2) along the transect defined on the IT propagation paths from sites A and D (Fig. 4).
1125 The horizontal gradient of the mean buoyancy frequency was strong near the topographic features (seamount and
1126 ridges; Figs. A1a-c) and the CE core (Fig. A1b), but quasi-uniform near the CE edge (Fig. A1c).



1127

1128 **Figure A1.** Horizontal gradient of the mean buoyancy frequency ($\nabla \overline{N^2}$) in the upper 200 m, shown along transects
1129 defined by the IT propagation paths from sites A and D (Fig. 4), for the (a) NE, (b) CEC, and (c) CEE cases. Color
1130 shading indicates the gradient magnitude. Notable topographic features are outlined by colored rectangles
1131 (seamount: green; ridges: magenta). Panels (b) and (c) also show the detected eddy edges for AE (yellow) and CE
1132 (cyan). All panels show selected potential density isopycnals (24–26 kg m⁻³, grey contours).

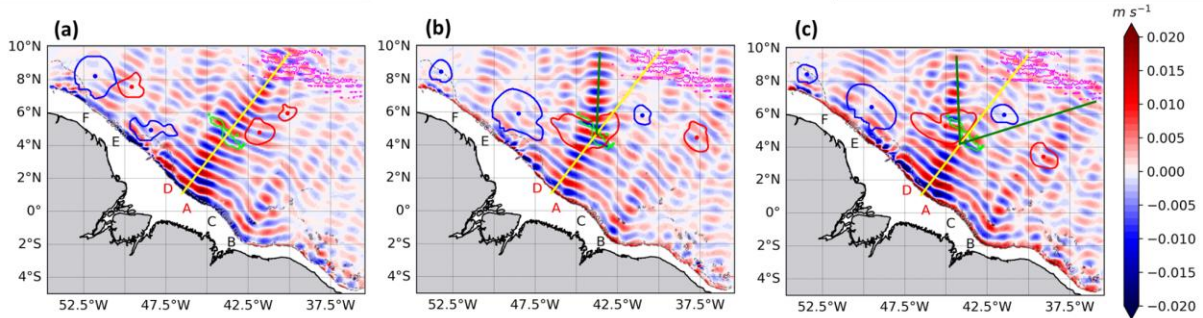
1133

1134 Appendix B: M₂ Tidal Beam Dynamics

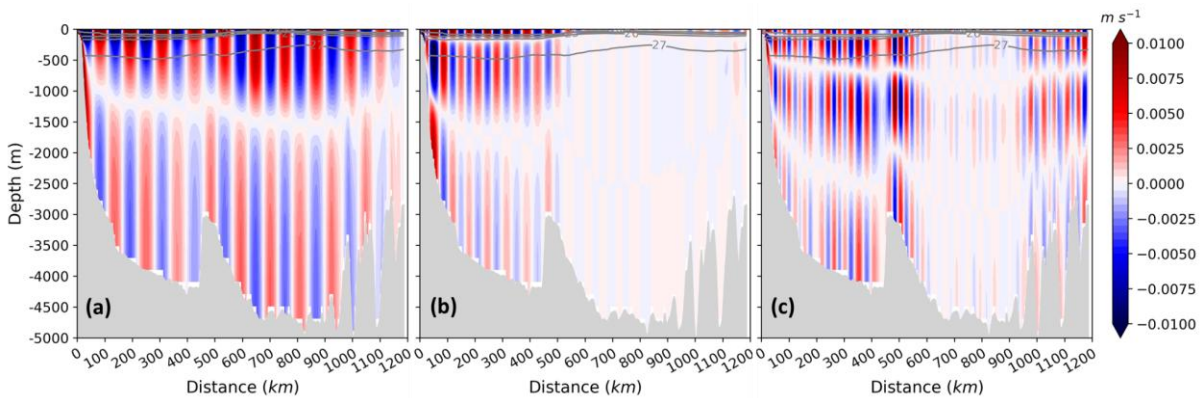
1135

1136 To better determine whether the response of ITs to MEs, specifically CEs, is governed more by the IT's vertical
1137 structure or by the CE's properties and location, we analyzed the M2 baroclinic velocity field. Following the
1138 methodology in Sect. 2.2.2, we projected the velocity field into vertical modes and defined transects along
1139 different IT beams for the NE, CEC, and CEE cases (Fig. B1): the northeastward incident beam (yellow) from
1140 sites A and D, northward refracted beams from CE center (green), and diffracted beams (northward and eastward)

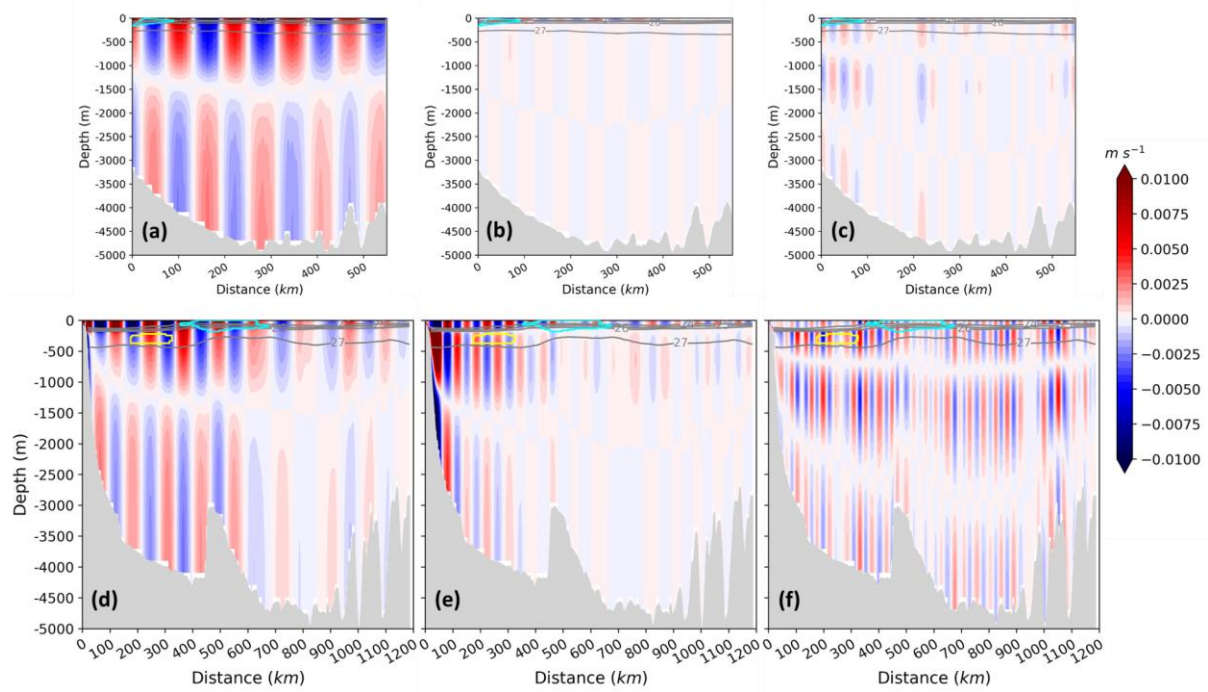
1141 from CE edge (green). We then decomposed the modal velocities into along- and cross-transect components. The
 1142 transect along the incident tidal beam was identical in all three cases to enable a direct comparison. Our analysis
 1143 focused on the more energetic along-transect component, as shown in Figs. B2-B4. The vertical structure of this
 1144 velocity component was found to be coherent with the modal M2 energy flux patterns in all analyzed cases.



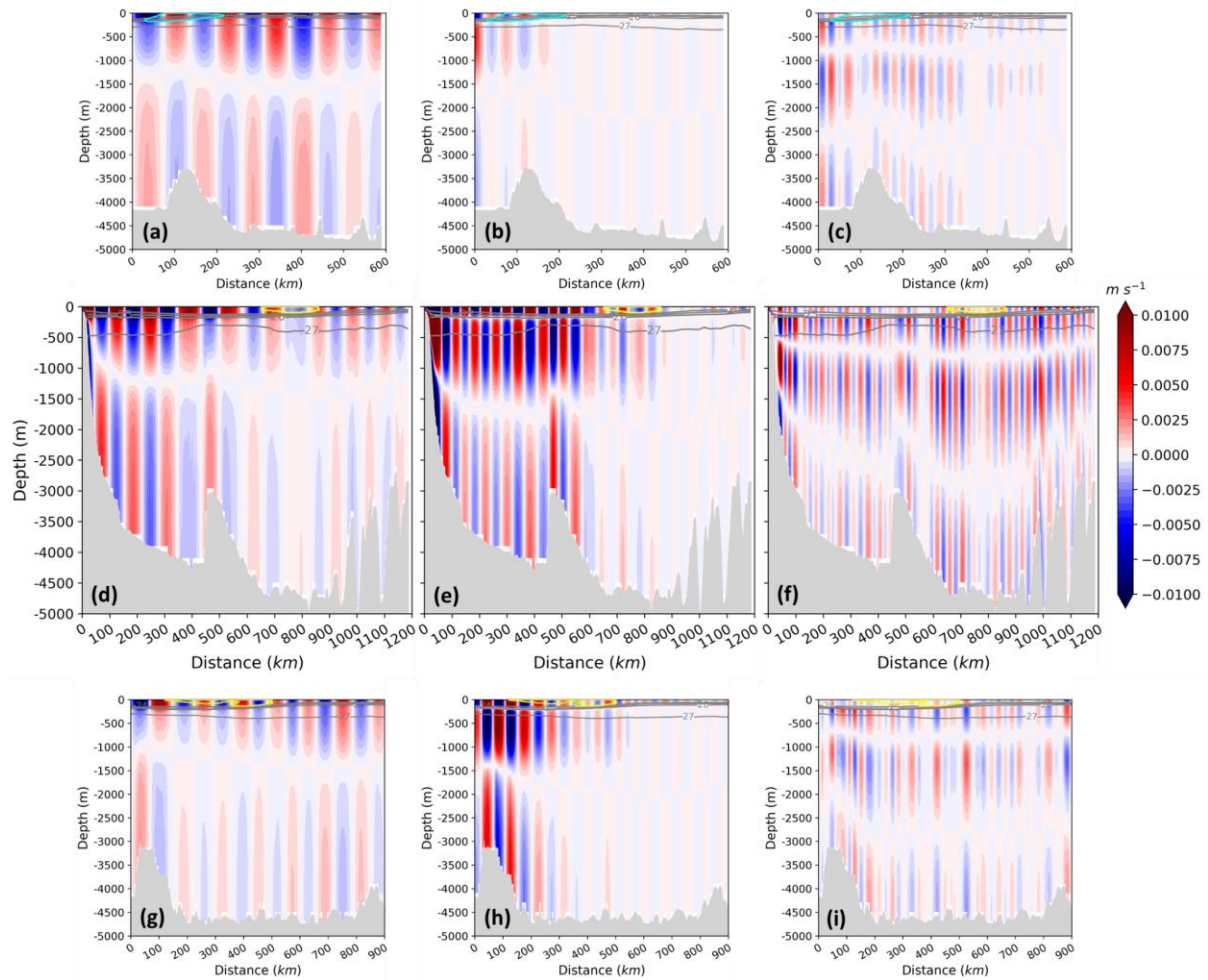
1145 **Figure B1.** Horizontal propagation of mode-1 M2 IT beams. Snapshots (at $t = 6$ h) of meridional baroclinic
 1146 velocity for the (a) NE, (b) CEC, and (c) CEE cases. The corresponding dates are 24 November 2015, 17
 1147 September 2015, and 29 September 2015, respectively. All panels include defined transects along different IT
 1148 beams: the northeastward incident beam (yellow lines) from sites A and D, northward refracted beams from CE
 1149 core (solid green line), and diffracted beams (northward and eastward) from CE edge (solid green lines). Detected
 1150 eddy edges (closed contours) and centroids (dots) for AE (blue) and CE (red) are also shown.
 1151



1152 **Figure B2.** Vertical structure of the first three M2 IT modes in the NE case. Snapshots ($t = 6$ h on 24 November
 1153 2015) of the along-transect baroclinic velocity component for modes 1 (a), 2 (b), and 3 (c) along the northeastward
 1154 incident beam. All panels include selected potential density isopycnals ($23\text{--}27\text{ kg m}^{-3}$, grey contours), and the
 1155 seafloor topography (grey shading).
 1156



1157
 1158 **Figure B3.** Vertical structure of the first three M2 IT modes in the CEC case. Snapshots ($t = 6$ h on 17 September
 1159 2015) of the along-transect baroclinic velocity component for modes 1 (a, d), 2 (b, e), and 3 (c, f) along different
 1160 beams: the northward diffracted beam (a-c) and the northeastward incident beam (d-f). All panels include detected
 1161 eddy edges for AE (yellow) and CE (cyan), selected potential density isopycnals ($23\text{--}27\text{ kg m}^{-3}$, grey contours),
 1162 and the seafloor topography (grey shading).



1163
 1164 **Figure B4.** Vertical structure of the first three M2 IT modes in the CEE case. Snapshots ($t = 6$ h on 29 September
 1165 2015) of the along-transect baroclinic velocity component for modes 1 (a, d, g), 2 (b, e, h), and 3 (c, f, i) along
 1166 different beams: the northward diffracted beam (a-c), the northeastward incident beam (d-f), and the eastward
 1167 diffracted beam (g-i). All panels include detected eddy edges for AE (yellow) and CE (cyan) eddies, selected
 1168 potential density isopycnals ($23\text{--}27\text{ kg m}^{-3}$, grey contours), and the seafloor topography (grey shading).
 1169